Article

Comprehensive Investigation of Thermal and Flow Features of Alloy Based Nanofluid Considering Shape and Newtonian Heating Effects via New Fractional Approach

Shah Muhammad [1], Talha Anwar [2,*], Asifa [3] and Mehmet Yavuz [4,*]

1 Department of Mathematics, College of Science, King Saud University, P.O. Box 2455, Riyadh 11451, Saudi Arabia
2 Center of Excellence in Theoretical and Computational Science (TaCS-CoE), Science Laboratory Building, Faculty of Science, King Mongkut's University of Technology Thonburi (KMUTT), 126 Pracha-Uthit Road, Bang Mod, Thung Khru, Bangkok 10140, Thailand
3 Department of Mathematics, Faculty of Science, King Mongkut's University of Technology Thonburi, 126 Pracha-Uthit Road, Bang Mod, Thung Khru, Bangkok 10140, Thailand
4 Department of Mathematics and Computer Sciences, Faculty of Science, Necmettin Erbakan University, Konya 42090, Turkey
* Correspondence: anwartalha80@gmail.com (T.A.); mehmetyavuz@erbakan.edu.tr (M.Y.)

Abstract: The core purpose of this work is the formulation of a mathematical model by dint of a new fractional modeling approach to study the dynamics of flow and heat transfer phenomena. This approach involves the incorporation of the Prabhakar fractional operator in mathematical analysis to transform the governing system from a conventional framework to a generalized one. This generalized model evaluates the improvement in thermal efficacy of vacuum pump oil because of the inclusion of aluminum alloy nanoparticles. The flow of the under-observation nanofluid starts due to the combined effects of natural convection and the ramped velocity function at the boundary. Meanwhile, an analysis of the energy equation is conducted by taking the Newtonian heating mechanism into consideration. The characteristics of platelet-, brick-, cylinder-, and blade-shaped alloy nanoparticles are incorporated into the primary system using shape-dependent relations for thermal conductivity and viscosity. Both the classical and generalized models are solved to derive the exact solutions by first inserting some dimension-independent quantities and then operating the Laplace transform on the succeeding equations. These solutions are utilized for the development of graphical illustrations to serve the purpose of covering all features of the problem under consideration. Furthermore, changes in energy and flow functions due to the dominant influences of the relevant contributing factors are delineated with appropriate physical arguments. In addition, the numerical results of the skin friction coefficient and Nusselt number are displayed via multiple tables to analyze the disturbance in shear stress and discuss the contribution of the fractional parameters, the volume concentration of the considered nanoparticles, and the shape factor in the boost of the thermal potential of the considered nanofluid. The findings imply that aluminum alloy nanoparticles have the ability to produce a 44% enhancement in the thermal effectiveness of vacuum pump oil. Moreover, the flow velocity is reduced as the loading range of the nanoparticles rises.

Keywords: Prabhakar fractional operator; shape factor; Newtonian heating; ramped velocity function; nanofluid; heat transfer

1. Introduction

In this contemporary era of innovations and development, the technological sector is concentrated on producing materials that are compact in terms of sizes and structures, but at the same time, they efficiently satisfy practical needs. In this context, nanotechnology is one of the most prominent fields, and in recent times, there have been significant advancements in this domain. Nanotechnology is the maneuvering of matter, adapting exclusive

strategies and methods to fabricate products at micro- and macro-scales for industrial and commercial purposes. Some of its most paramount peculiarities that have drawn the fascination of scientists are the efficient employment of resources, reduced fabrication outlay, lower time consumption, better performances of developed products, and consequently ameliorated standards of living. It offers scientific progress and leads the way toward the development of innovative technologies across several industries, including the pharmaceutical industry, energy sector, automobile manufacturing, nanoelectronics, and mechanical engineering, just to name a few [1,2]. In addition, consumer products, tissue engineering, elimination of cancer cells, cleansing of blood arteries, expeditious healing of cuts via the infusion of silver with bandages, and preparation of electronic devices that consume less power are cost-efficient and possess better displays, production of improved construction items, paints, furniture polishes, household appliances, and manufacturing of long-lasting and more durable products are some of the prominent areas where nanotechnology contributes significantly.

Nanofluid is a fundamental feature of nanotechnology, and one of its primary functions is to efficiently handle heat transfer challenges. The speedy disposal of redundant heat is one of the main obstacles to the efficacious performance of several industrial and household equipment such as energy storage instruments, computer processors, heat exchangers, refrigerators, thermal plants, solar collectors, and so forth. The thermal propensities of pure fluids involved in such systems are inadequate; therefore, experts have proposed an assortment of approaches to strengthen their thermal effectiveness in order to serve the purpose of achieving appropriate thermal management of exceptionally sensitive operations. In this regard, a substantial change has been caused by the development of nanofluid, which accelerates the rates at which heat is transported while simultaneously enhancing the anti-wear and corrosion resistance attributes of standard fluids. In general, solid particles composed of nitrides (silicon nitrides, aluminum nitrides), metal oxides (CO_2, silica), metals (copper, zinc, iron), and non-metals (carbon nanotubes, graphite) are dispersed in standard fluids such as kerosene oil, blood, lubricants, and water for the preparation of nanofluids [3]. These solid particles are below 100 nanometers in terms of size. At this nanoscale, the materials begin to exhibit distinctive properties that have a momentous impact on the biological, physical, and chemical behaviors of carrier fluids. In comparison to standard fluids, nanofluids are more efficient when it comes to the transportation of heat. Numerous advantageous effects of amalgamating nanoparticles with standard fluids, for instance, improved tribological efficacy, diminished parasitic loss, enhanced lubrication capacity, and boosted cooling performance, endorse nanofluids as a beneficial substitute for standard fluids in various practical functions such as pharmaceutical operations, optical sensors, combustion plants, grinding processes, nuclear reactors, high-temperature drilling, cooling of microchips, and many others.

Multiple new disciplines of science and technology, including nanochemistry and nanoelectronics, have emerged after the recognition of nanofluids. Recently, various researchers across the globe arranged analytic and experimental studies to discuss the efficiency of nanofluids in complicated physical situations. Wen et al. [4] proposed a new algorithm to estimate the Nusselt number of water–ZnO nanofluid for flow in mini-channels. Based on their experimental analysis, they remarked that the pressure drop and heat-transportation rate are higher in the case of nanofluids as equated to those of pure fluids. Rizwan et al. [5] compared the performances of three ethylene glycol-based nanofluids and analyzed the effects of variations in diameter and proportion. They discussed that, in response to diameter enhancement, the temperature increases and the flow becomes decelerated, whereas a reverse behavior was reported when the proportion of nanoparticles rises in the base fluid. Sarwar and Hussain [6] evaluated the flow features of a blood- and silver-based nanofluid and concluded that an expansion in the size of silver particles expedites the blood flow and escalates the temperature. Wang et al. [7] considered round- and triangular-shaped heat exchangers and examined their performance in the presence of a silica–water nanofluid. They communicated that the efficiency of

heat exchangers rises 74.80% for round tubes and 55.97% for triangular tubes because of the considered nanofluid. The impacts of the diameter and nanolayer on the thermal behavior of a nanofluid containing graphene and water were studied by Acharya et al. [8]. They claimed a 84.61% augmentation in thermal performance for the flow induced due to the spinning motion of a magnetized disk. To compare the heat-transportation potential of γAl_2O_3–water and γAl_2O_3–ethylene glycol nanofluids, Salahuddin et al. [9] used experimental relations for the estimation of viscous influences and thermal conductance. Their results explain that γAl_2O_3 nanoparticles have a crucial contribution in strengthening the thermal traits of ordinary fluids. Some recent analyses in the field of nanofluids are documented in [10–14].

The natural flow and thermal attributes of the carrier fluid and volume concentration, size, shapes, and types of nanoparticles are some of the most indispensable variables that control the overall productivity and usability of nanofluids. When these factors are taken into consideration, the question of which shape of nanoparticles is highly beneficial for gaining the maximum boost in thermal properties and, as a result, improved thermal effectiveness and stability, emerges as a significant issue. A meticulous analysis of the literature indicates that only a few studies have been conducted in this regard, which shows that this topic has not gained much attention. However, it is crucial to understand that leaving out the shape factor in theoretical investigations reduces the practical relevance of the presented results. Waqas et al. [15] examined the importance of differently shaped gold nanoparticles for the thermal behavior of blood. They predicted the escalation in the performance of blood due to sphere, hexahedron, cylinder, column, and tetrahedron shapes of nanoparticles. Alqaed et al. [16] conducted a numerical analysis to scrutinize the influences of the shape factor on entropy generation. They combined alumina boehmite nanoparticles of diverse shapes with water and evaluated the thermal efficiency of the resulting nanofluid for flow in heat sinks. Saranya and Al-Mdallal [17] investigated the flow of alumina- and silicon oil-based nanofluid around a radially extending and rotating surface to observe the contribution of radiative energy, magnetic force, and shape diversity of nanoparticles in the development of flow and thermal fields. A comparative discussion on entropy production and Nusselt number for needle-, sphere-, and disk-shaped nanoparticles was presented by Ellahi et al. [18]. They noted that the needle-like shape of nanoparticles leads to producing the maximum entropy generation and the highest thermal profile. Saqib et al. [19] considered the Brinkman model and conducted a theoretical study in a fractional setting to elucidate the control of shape effects on the thermal conduct of nanofluid. They computed the exact solutions of the model and provided several graphs in support of their results. A comprehensive review of shape effects on the thermal efficacy of nanofluids was provided by Zahmatkesh et al. [20]. They covered cavity flows, boundary layer flows, flows in heat exchangers and channels, and peristaltic flows. Some latest findings regarding the shapes of nanoparticles can be observed from [21–25].

Fractional calculus is a rapidly growing new discipline, and the concept of generalizing standard models by dint of various fractional techniques is attributed for the existence of this field. Recently, a number of researchers have modeled several physical problems in fractional settings and carried out comparative studies. Based on their analyses, they claimed that the precision and reliability of the results obtained in fractional frameworks are relatively higher than those acquired in classical settings. Furthermore, they provide a better and more accurate description of the problems being modeled. Such recommendations are further supported by the observation that an accurate accordance between the experimental reports and the theoretic results produced through such fractional systems can be established by appropriately modulating the fractional parameters. The aforementioned supplementary advantages of fractional modeling techniques have motivated a vast range of scientists to organize comparative investigations in fractional and conventional environments. Since the performance of a system at a particular level depends on its history and current state, fractional models are more suitable to explain such performances because they address the inherited features of the involved materials, self-similar attributes,

and memory effects. These characteristics of fractional models are also effective for the profound comprehension of viscoelastic impacts and the rheology of nanofluids. Hence, the models developed operating fractional techniques are more efficient in terms of describing the thermal behavior and flow patterns of nanofluids. In recent times, dynamical systems, mathematical biology, thermal engineering, disease modeling, flows in cavities and porous mediums, and economics are some of the various disciplines where fractional models are being applied in full swing.

Numerous fractional operators have been developed to date, each having a unique formulation, advantages, and limitations. The operators regarded as Riemann–Liouville and Caputo are particularly prevalent [26]. The development of the foregoing operators includes the convolution of the first derivative and a kernel based on the power-law. Caputo–Fabrizio is another frequently employed derivative, whose mathematical relation involves the convolution of an exponential kernel and the standard derivative [27]. To efficaciously tackle the locality and singularity problems appearing when the aforesaid derivatives are used for the formulation of models, a new derivative comprised of the generalized Mittag–Leffler function was proposed by Atangana and Baleanu [28]. Later, the Prabhakar fractional operator was introduced, which contains a multi-parametric Mittag–Leffler function as a kernel [29]. Various modern-day researchers are fascinated by the significant properties of fractional operators, thus they prefer fractional modeling techniques. So far, a plethora of physical problems from diverse fields have been examined and delineated by means of fractional models. Danane et al. [30] formulated a fractional model to investigate the impacts of government measurements and the public's risk awareness on controlling the outbreak of COVID-19. They worked with actual data collected in Wuhan and also incorporated zoonotic and person-to-person transmission effects in their model. Akgul et al. [31] employed different fractional approaches to construct economic models. They provided numerical schemes to estimate the solutions of these models and performed comparative studies. A detailed report on how different fractional operators can be used to comprehend and elucidate the thermal performance and flow behavior of fluids was supplied by Siddique et al. [32]. Chen et al. [33] evaluated the influences of the slip velocity condition on the flow patterns of Oldroyd-B fluid by generalizing Fick's and Fourier's law via the Prabhakar fractional operator. Raza et al. [34] discussed the contribution of inclined magnetic effects in varying the flow characteristics of viscous fluids. For this study, they implemented a fractional model, which is based on a multi-parametric kernel. Some new reports on modeling flow problems via fractional approaches are available in [35–38].

A lack of investigations on oil-based nanofluids is found through a critical analysis of the literature. The majority of these studies were conducted via classical models, and solution approximation techniques were operated for the development of graphs. Thus, the research gap further expands if the derivation of analytic solutions employing fractional models is taken into consideration. In addition, it is observed that most of these investigations communicate results only for spherically shaped nanoparticles, excluding the influence of the shape factor. In the physical sense, the shape factor has a vital role regarding the thermal performance and behavior of nanofluids. Therefore, this work is an attempt to effectively address all these issues. The primary focus of this study is to anticipate how the dispersion of differently shaped aluminum alloy nanoparticles (brick, platelet, blade, and cylinder) affects the thermal efficiency and flow characteristics of vacuum pump oil. The performance of vacuum pump oil in the presence of alloy nanoparticles is being evaluated for the first time in this study. The formulation of a generalized model and the computation of exact solutions are also the main objectives of this investigation. The Prabhakar fractional operator is utilized to serve the former objective, and to solve the consequent system of equations, the Laplace transform is exercised. The fractional model corresponds to Newtonian heating and ramped velocity conditions. The solutions are provided graphically to examine the importance of the involved parameters regrading percentage augmentation in heat-transportation rate, shear stress, and flow patterns. Furthermore, the primary

functions (velocity and temperature) established for the fractional case are compared with those of the classical case to highlight the significance of fractional models.

2. Statement and Model Formulation

This investigation is performed to analyze how the distribution of aluminum alloy nanoparticles possessing multiple shapes ameliorates the thermal and physical attributes of vacuum pump oil. The consideration of a ramped velocity relation at the bounding surface causes the instigation of flow. Newtonian heating phenomena disrupt the system initially for $t^* = 0^+$. The mathematical representation of this mechanism is composed of an energy gradient and a temperature function, whereas the bounding surface is assumed to execute a ramped motion. This type of motion is described through a piecewise function, which contains time-dependent and constant parts. It indicates that the velocity depends on time for a certain time duration ($t^* \leq t_0$) such that $V^*(t^*, 0) = V_0(t^*/t_0)$. Afterward, for $t^* > t_0$, the bounding surface achieves constant velocity V_0. At the far end, ambient temperature $\top_\infty$ is achieved and the nanofluid comes to a rest. Since the flow is unidirectional and the vertical bounding surface is sufficiently long, the only independent variables in the thermal and velocity equations are Y^* and t^*. This study is focused on platelet-, brick-, cylinder-, and blade-type shapes of aluminum alloy nanoparticles, and a thermal equilibrium is supposed to exist between the host fluid and dispersed particles. The geometrical configuration and considered shapes of nanoparticles are portrayed in Figure 1.
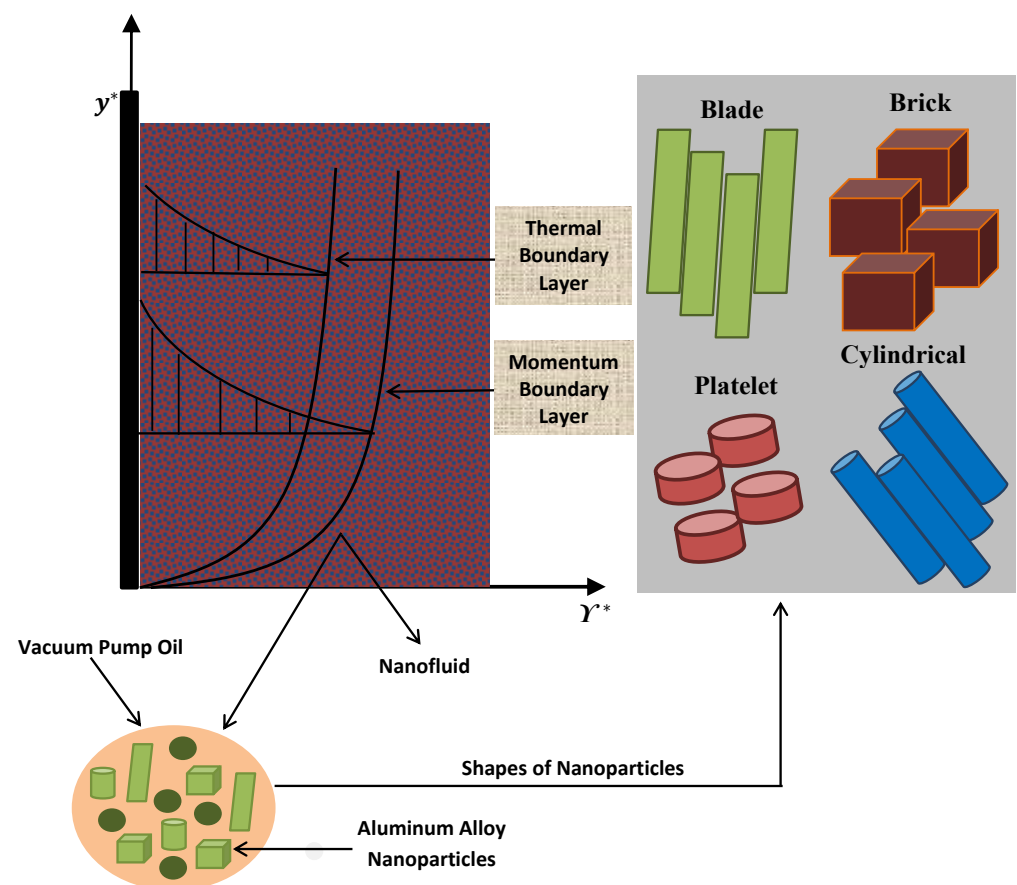

Figure 1. Geometrical arrangement of the problem.

Keeping view of the above description and taking Boussinesq's approximation into account, the principal model for this problem is formulated as [39]

$$(1 + \lambda_1)\widehat{\rho}_{nf}\frac{\partial V^*(t^*, Y^*)}{\partial t^*} = \widehat{\mu}_{nf}\left(1 + \lambda_0\frac{\partial}{\partial t^*}\right)\frac{\partial^2 V^*(t^*, Y^*)}{\partial Y^{*2}} + (1 + \lambda_1)(\widehat{\rho\beta})_{nf}(\top(t^*, Y^*) - \top_\infty)g, \tag{1}$$

$$(\widehat{\rho}\widehat{\mathcal{C}}_p)_{nf}\frac{\partial \top^*(t^*, Y^*)}{\partial t^*} = -\frac{\partial q^*(t^*, Y^*)}{\partial Y^*}, \tag{2}$$

$$q^*(t^*, Y^*) = -\widehat{\mathcal{K}}_{nf}\frac{\partial \top^*(t^*, Y^*)}{\partial Y^*}. \tag{3}$$

The initial and boundary conditions associated with the above system are described as

$$V^*(0, Y^*) = 0, \quad \top^*(0, Y^*) = \top_\infty, \quad \text{for} \quad Y^* > 0, \tag{4}$$

$$V^*(t^*, 0) = \begin{cases} V_0\frac{t^*}{t_0} & 0 < t^* \le t_0 \\ V_0 & t^* > t_0 \end{cases}, \quad \left(\frac{h}{\widehat{\mathcal{K}}_{nf}}\right)\top(t^*, 0) = -\frac{\partial \top^*(t^*, 0)}{\partial Y^*}, \tag{5}$$

$$V^*(t^*, Y^*) \to 0, \quad \top(t^*, Y^*) \to \top_\infty, \quad \text{as} \quad Y^* \to \infty, \tag{6}$$

where q^* is the thermal flux, V_0 symbolizes the reference velocity, h specifies the heat transport coefficient, the energy and flow functions are represented by $\top^*$ and V^*, the pull of gravity is characterized by g, $\top_\infty$ denotes the ambient temperature, $\lambda_{i=0,1}$ are specific parameters associated with Jeffery fluids, and the characteristic time t_0 is defined as $t_0 = \frac{1}{\widehat{v}_{\text{VPO}}}\left(\frac{\widehat{\mathcal{K}}_{\text{VPO}}}{h}\right)^2$. The mathematical form of the physical and thermal characteristics of the considered nanofluid is presented as [40,41]

Thermal conductivity:

$$\widehat{\mathcal{K}}_{nf} = \left\{\frac{\varphi(\alpha - 1)(\widehat{\mathcal{K}}_{\text{ANP}} - \widehat{\mathcal{K}}_{\text{VPO}}) + \widehat{\mathcal{K}}_{\text{ANP}} + (\alpha - 1)\widehat{\mathcal{K}}_{\text{VPO}}}{\varphi(\widehat{\mathcal{K}}_{\text{VPO}} - \widehat{\mathcal{K}}_{\text{ANP}}) + \widehat{\mathcal{K}}_{\text{ANP}} + \widehat{\mathcal{K}}_{\text{VPO}}(\alpha - 1)}\right\}\widehat{\mathcal{K}}_{\text{VPO}}$$

Viscosity:

$$\widehat{\mu}_{nf} = \widehat{\mu}_{\text{VPO}}\left(1 + \kappa_1\varphi + \kappa_1\varphi^2\right)$$

Specific heat capacity:

$$(\widehat{\rho}\widehat{\mathcal{C}}_p)_{nf} = (\widehat{\rho}\widehat{\mathcal{C}}_p)_{\text{VPO}}\left[1 - \varphi\left\{1 - \frac{(\widehat{\rho}\widehat{\mathcal{C}}_p)_{\text{ANP}}}{(\widehat{\rho}\widehat{\mathcal{C}}_p)_{\text{VPO}}}\right\}\right]$$

Thermal expansion coefficient:

$$\left(\widehat{\rho}\widehat{\beta}\right)_{nf} = \left(\widehat{\rho}\widehat{\beta}\right)_{\mathrm{VPO}}\left[1 - \varphi\left\{1 - \frac{\left(\widehat{\rho}\widehat{\beta}\right)_{\mathrm{ANP}}}{\left(\widehat{\rho}\widehat{\beta}\right)_{\mathrm{VPO}}}\right\}\right]$$

Density:

$$\widehat{\rho}_{nf} = \widehat{\rho}_{\mathrm{VPO}}\left[1 - \varphi\left\{1 - \frac{\widehat{\rho}_{\mathrm{ANP}}}{\widehat{\rho}_{\mathrm{VPO}}}\right\}\right]$$

In the above expressions of thermo-physical characteristics, the subscripts "VPO", "ANP", and "nf" denote the association of specific properties with vacuum pump oil, aluminum alloy nanoparticles, and the consequent nanofluid, respectively. The loading range of nanoparticles is characterized by φ. The parameter α in the expression for thermal conductivity is the shape factor, which plays a vital part in improving the heat transfer capacity of the base fluid. The values of α for the considered shapes of nanoparticles are displayed in Table 1. The respective table also provides values for κ_1 and κ_2, which significantly affect the viscous nature of the base fluid.

Table 1. Values of α, κ_1, and κ_2 for multiple shapes of nanoparticles [42].

Shapes	κ_1	κ_2	α
Blade	14.6	123.3	8.3
Platelet	37.1	612.6	5.7
Brick	1.9	471.4	3.7
Cylinder	13.5	909.4	4.9

3. Generalization of the Model and Mathematical Analysis

The prime focus of this section is to present the generalization of the governing model in terms of the Prabhakar fractional derivative and then to compute the exact solutions of the consequent equations. The well-known Laplace transformation technique will be taken into consideration for the achievement of the latter purpose. Furthermore, mathematical expressions for some fundamental quantities of practical fascination will be provided in this section. Before the generalization of the governed model, the following unit-free parameters will be introduced in the energy and flow equations:

$$Y = \left(\frac{h}{\widehat{\mathcal{K}}_{\mathrm{VPO}}}\right)Y^*, \quad V = \frac{V^*}{V_0}, \quad q = \left(\frac{1}{h\top_\infty}\right)q^*,$$

$$t = \frac{\widehat{\mu}_{\mathrm{VPO}}}{\widehat{\rho}_{\mathrm{VPO}}}\left(\frac{h}{\widehat{\mathcal{K}}_{\mathrm{VPO}}}\right)^2 t^*, \quad \top = \frac{\top^* - \top_\infty}{\top_\infty}. \tag{7}$$

The unit-independent versions of the flow and temperature equations and their connected conditions are acquired in the following form:

$$\xi_1(1+\lambda_1)\frac{\partial V(t,Y)}{\partial t} = \xi_2 G_r(1+\lambda_1)\top(t,Y) + \xi_3\left(1+\lambda_2\frac{\partial}{\partial t}\right)\frac{\partial^2 V(t,Y)}{\partial Y^2}, \tag{8}$$

$$(Pr\xi_4)\frac{\partial\top(t,Y)}{\partial t} = -\frac{\partial q(t,Y)}{\partial Y}, \tag{9}$$

$$q(t,Y) = -\xi_5\frac{\partial\top(t,Y)}{\partial Y}, \tag{10}$$

$$\text{for}\quad Y>0:\quad \top(0,Y,)=0,\quad V(0,Y)=0, \tag{11}$$

$$V(t,0)=\begin{cases} t & 0<t\le 1 \\ 1 & t>1 \end{cases},\quad \frac{1}{\xi_5}\Big[1+\top(t,0)\Big]+\frac{\partial\top(t,0)}{\partial Y}=0, \tag{12}$$

$$\text{for}\quad Y\to\infty:\quad \top(t,Y)\to 0,\quad V(t,Y)\to 0. \tag{13}$$

The parameters depending on the volume fraction of nanoparticles and other parameters emerging in Equations (8)–(13) are given in Table 2. To transmute the model from the classical setting to the fractional setting, we operated the Prabhakar fractional derivative, which utilizes the generalized Fourier law to cope with heat flux. The generalized mathematical expression of the Fourier law for this problem is provided as

$$q(t,Y)=-\xi_5\left[\mathsf{D}^{\psi}_{\eta,\Omega,a}\frac{\partial\top(t,Y)}{\partial Y}\right]. \tag{14}$$

Let $C^y(0,n)$ represent the set of those functions, which have continuous derivatives of order $(y-1)$ on the interval $(0,n)$ such that, for an arbitrary function $\mathcal{H}\in C^y(0,n)$, $\mathcal{H}^{(y-1)}(\omega)$ is an absolutely continuous function. Considering of the above statement, the mathematical interpretation of the Prabhakar fractional derivative is supplied as [43]

$$\mathsf{D}^{\psi}_{\eta,\Omega,a}\{\mathcal{H}(\omega)\} = E^{-\psi}_{\eta,y-\Omega,a}\mathcal{H}^{(y)}(\omega) = e^{-\psi}_{\eta,y-\Omega}(a;\omega)*\mathcal{H}^{(y)}(\omega)$$

$$= \int_0^\omega (\omega-t)^{y-\Omega-1}E^{-\psi}_{\eta,y-\Omega}(a(\omega-t)^\eta)\mathcal{H}^y(t)dt, \tag{15}$$

where the integer part of Ω is symbolized as y such that $y=[\Omega]$. In Equation (15), the Prabhakar kernel, Prabhakar integral, and Mittag–Leffler function for multiple parameters are, respectively, provided as [44]

$$e^{\psi}_{\eta,\Omega}(a;\omega)=\omega^{\Omega-1}E^{\psi}_{\eta,\Omega}(a\omega^\eta),$$

$$E^{\psi}_{\eta,\Omega,a}\mathcal{H}(\omega)=\int_0^\omega (\omega-t)^{(\Omega-1)}E^{\psi}_{\eta,\Omega}(a(\omega-t)^\eta)\mathcal{H}(t)dt,$$

$$E^{\psi}_{\eta,\Omega}(r)=\sum_{m=0}^{\infty}\frac{r^m\Gamma(m+\psi)}{m!\Gamma(\psi)\Gamma(\Omega+\eta m)}. \tag{16}$$

Since the Laplace transform is considered in this work as a primary tool to derive the exact solutions of the under-observation model, therefore, before directly applying it to the generalized equations, it is important to mention the Laplace transformed version of the Prabhakar fractional derivative. Thus, the Laplace transform will be applied to the Prabhakar fractional derivative in the following manner:

$$
\begin{aligned}
\mathcal{L}\left[\mathrm{D}_{\eta,\Omega,a}^{\psi}\{\mathcal{H}(\omega)\}\right] &= \mathcal{L}\left[e_{\eta,y-\Omega}^{-\psi}(a;\omega) * \mathcal{H}^{(y)}(\omega)\right] \\
&= \mathcal{L}\left[e_{\eta,y-\Omega}^{-\psi}(a;\omega)\right]\mathcal{L}\left[\mathcal{H}^{(y)}(\omega)\right] \\
&= p^{\Omega-y}(1-ap^{-\eta})^{\psi}\,\mathcal{L}\left[\mathcal{H}^{y}(\omega)\right].
\end{aligned}
\tag{17}
$$

Table 2. Parameters appearing in Equations (8)–(13).

Symbols	Parameters	Mathematical Relations
P_r	Prandtl number	$\left(\frac{\hat{c}_p\hat{\mu}}{\hat{\mathcal{K}}}\right)_{\mathrm{VPO}}$
λ_2	Jeffery parameter	$\lambda_0(\hat{\nu}_{\mathrm{VPO}})\left(\frac{h}{\hat{\mathcal{K}}_{\mathrm{VPO}}}\right)^2$
G_r	Grashof number	$\left(\frac{\hat{\mathcal{K}}_{\mathrm{VPO}}}{h}\right)^2\frac{g\top_\infty}{V_0}\left(\frac{\hat{\beta}}{\hat{\nu}}\right)_{\mathrm{VPO}}$
ξ_1		$\left[1-\varphi\left(\frac{\hat{\rho}_{\mathrm{VPO}}-\hat{\rho}_{\mathrm{ANP}}}{\hat{\rho}_{\mathrm{VPO}}}\right)\right]$
ξ_2	Parameters depending on	$\left[1-\varphi\left\{\frac{(\hat{\rho}\hat{\beta})_{\mathrm{VPO}}-(\hat{\rho}\hat{\beta})_{\mathrm{ANP}}}{(\hat{\rho}\hat{\beta})_{\mathrm{VPO}}}\right\}\right]$
ξ_3	volume proportion	$(1+\kappa_1\varphi+\kappa_2\varphi^2)$
ξ_4	of nanoparticles	$\left[1-\varphi\left\{\frac{(\hat{\rho}\hat{c}_p)_{\mathrm{VPO}}-(\hat{\rho}\hat{c}_p)_{\mathrm{ANP}}}{(\hat{\rho}\hat{c}_p)_{\mathrm{VPO}}}\right\}\right]$
ξ_5		$\frac{\varphi(\alpha-1)(\hat{\mathcal{K}}_{\mathrm{ANP}}-\hat{\mathcal{K}}_{\mathrm{VPO}})+\hat{\mathcal{K}}_{\mathrm{ANP}}+(\alpha-1)\hat{\mathcal{K}}_{\mathrm{VPO}}}{\varphi(\hat{\mathcal{K}}_{\mathrm{VPO}}-\hat{\mathcal{K}}_{\mathrm{ANP}})+\hat{\mathcal{K}}_{\mathrm{ANP}}+\hat{\mathcal{K}}_{\mathrm{VPO}}(\alpha-1)}$

3.1. Solution for Fractional Temperature Distribution

The application of the Laplace transform on the generalized Fourier law (Equation (14)), energy equation (Equation (9)), and corresponding conditions (Equations (12) and (13)) yields the following system for the temperature field:

$$
q(p,Y) = -\xi_5\left\{\frac{p^\Omega}{(1-ap^{-\eta})^{-\psi}}\right\}\frac{d\top(p,Y)}{dY},
\tag{18}
$$

$$
p\{\top(p,Y)\} = -\left(\frac{1}{P_r\xi_4}\right)\frac{dq(p,Y)}{dY},
\tag{19}
$$

$$
-\frac{1}{\xi_5}\left[\frac{1}{p}+\top(p,0)\right] = \frac{d\top(p,0)}{dY} \quad \text{and} \quad \top(p,Y)\to 0 \quad \text{for} \quad Y\to\infty.
\tag{20}
$$

Here, first we substitute Equation (18) in Equation (19) after taking its derivative, and then we perform some simplification steps to obtain the following expression:

$$
\frac{d^2\top(p,Y)}{dY^2}-\left[\frac{P_r\xi_4}{\xi_5}\left\{\frac{p}{p^\Omega(1-ap^{-\eta})^{\psi}}\right\}\right]\top(p,Y) = 0.
\tag{21}
$$

The solution of Equation (21) with respect to the conditions provided in Equation (20) is determined as

$$\top(p, Y) = \frac{1}{p\left(\sqrt{\frac{p(\xi_4\xi_5)P_r}{p^\Omega(1 - ap^{-\eta})^\psi}} - 1\right)} \exp\left(-\sqrt{\frac{p(\xi_4\xi_5)P_r}{p^\Omega(1 - ap^{-\eta})^\psi}} Y\right). \tag{22}$$

Equation (22) is quite complex, and its transformation to the real-domain is not possible from the current form. To handle this problem effectively, we assigned new parameters to some complicated expressions of the above equation as follows:

$$\top_0(p, Y) = \frac{\exp\left(-\sqrt{f_0(p)}Y\right)}{\sqrt{f_0(p)} - 1} \quad \text{and} \quad f_0(p) = \frac{p(\xi_4\xi_5)P_r}{p^\Omega(1 - ap^{-\eta})^\psi}. \tag{23}$$

The Laplace inversion of an arbitrary function of the following form,

$$f_1(p, Y) = \frac{\exp(-\sqrt{p}Y)}{\sqrt{p} - 1}, \tag{24}$$

is supplied as

$$f_1(t, Y) = e^{(t-Y)} \operatorname{erfc}\left(\frac{Y}{\sqrt{4t}} - \sqrt{t}\right) + \left\{\left(\pi t^2\right)^{-1/2}\right\} e^{\left(-\frac{Y^2}{4t}\right)}. \tag{25}$$

For the under-observation problem, $\top_0(p, Y) = f_1(f_0(p), Y)$. Thus, the inverse transformation of the function $\top_0(p, Y)$ is computed as

$$\top_0(t, Y) = \int_0^\infty f_1(\zeta, Y) f_2(t, \zeta) d\zeta, \tag{26}$$

where

$$f_2(t, \zeta) = \sum_{n=0}^\infty \frac{(-P_r(\xi_4\xi_5)\zeta)^n}{n!} t^{(\Omega-1)n-1} E_{\eta,(\Omega-1)n}^{n\psi}(at^\eta). \tag{27}$$

The inverse transformation of the energy function $(\top(p, Y))$ to the real coordinates $((t, Y))$ is performed in light of Equations (23)–(27) as follows:

$$\top(t, Y) = H(t) * \top_0(t, Y) = \int_0^t \top_0(z, Y) dz. \tag{28}$$

Here, $H(t)$ symbolizes the Heaviside step function and * denotes the convolution product.

3.2. Solution for Classical Temperature Distribution

In order to compare the results for the generalized and standard frameworks, the solution of the energy equation is also derived by using the classical Fourier law. The final form of this solution in the Laplace domain is presented as

$$\top(p,Y) = \left\{ \frac{\check{\xi}_6}{\sqrt{p} - \frac{1}{\sqrt{(\check{\xi}_4\check{\xi}_5)P_r}}} \right\} \frac{\exp\left(-\sqrt{p(\check{\xi}_4\check{\xi}_5)P_rY}\right)}{p}. \tag{29}$$

After operating the Laplace inversion on Equation (29), the energy function is transformed back to the real-domain as

$$\top(t,Y) = \check{\xi}_6 f_3(t) * \text{erfc}\left(\frac{\sqrt{(\check{\xi}_4\check{\xi}_5)P_r}Y}{\sqrt{4t}} \right), \tag{30}$$

where

$$f_3(t) = \pi^{-1/2} t^{-1/2} + \frac{\exp\left(\frac{t}{(\check{\xi}_4\check{\xi}_5)P_r}\right)}{\sqrt{(\check{\xi}_4\check{\xi}_5)P_r}} \text{erfc}\left(-\frac{\sqrt{t}}{\sqrt{(\check{\xi}_4\check{\xi}_5)P_r}} \right), \quad \check{\xi}_6 = \frac{1}{\sqrt{(\check{\xi}_4\check{\xi}_5)P_r}}. \tag{31}$$

3.3. Solution for Fractional Velocity Distribution

To determine the solution of the flow equation, the Laplace transform is applied to Equation (8) and the respective conditions given in Equations (12) and (13). The Laplace domain system for the flow field is established as

$$\xi_1(1+\lambda_1)pV(p,Y) = \xi_2(1+\lambda_1)G_r\top(p,Y) + \xi_3(1+\lambda_2p)\frac{d^2V(p,Y)}{dY^2}, \tag{32}$$

$$V(p,0) = -\frac{e^{-p}}{p^2} + \frac{1}{p^2} \quad \text{and} \quad V(p,Y) \to 0 \quad \text{for} \quad Y \to \infty. \tag{33}$$

After substituting the value of the energy function ($\top(p,Y)$) from Equation (22), Equation (32) takes the following form:

$$\{\xi_1(1+\lambda_1)p\}V(p,Y) = \frac{\xi_2(1+\lambda_1)G_r}{p\left(\sqrt{\frac{p(\check{\xi}_4\check{\xi}_5)P_r}{p^\Omega(1-ap^{-\eta})^\psi}} - 1\right)} \exp\left(-\sqrt{\frac{p(\check{\xi}_4\check{\xi}_5)P_r}{p^\Omega(1-ap^{-\eta})^\psi}}Y\right)$$

$$+ \{\xi_3(1+\lambda_2p)\}\frac{d^2V(p,Y)}{dY^2}. \tag{34}$$

Further simplification of the above equation for the convenient determination of the exact solution yields

$$\frac{d^2V(p,Y)}{dY^2} = \frac{\xi_1}{\xi_3}\left\{ \frac{(1+\lambda_1)p}{(1+\lambda_2p)} \right\}V(p,Y)$$

$$- \left\{ \frac{\xi_2(1+\lambda_1)G_r}{\xi_3(1+\lambda_2p)} \right\} \frac{1}{p\left(\sqrt{\frac{p(\check{\xi}_4\check{\xi}_5)P_r}{p^\Omega(1-ap^{-\eta})^\psi}} - 1\right)} \exp\left(-\sqrt{\frac{p(\check{\xi}_4\check{\xi}_5)P_r}{p^\Omega(1-ap^{-\eta})^\psi}}Y\right). \tag{35}$$

On solving Equation (35), in light of the conditions provided in Equation (33), we obtain the following expression for the flow function:

$$V(p,Y) = \left(-\frac{e^{-p}}{p^2} + \frac{1}{p^2}\right)\exp\left(-\sqrt{\frac{p(1+\lambda_1)\xi_1}{\xi_3(1+\lambda_2 p)}}Y\right)$$

$$+ \frac{\xi_7 G_r\left(\sqrt{f_0(p)}-1\right)^{-1}}{p\{\xi_8(1+\lambda_2 p)f_0(p)-p\}}\left[\exp\left(-\sqrt{\frac{p(1+\lambda_1)\xi_1}{\xi_3(1+\lambda_2 p)}}Y\right) - \exp\left(-\sqrt{f_0(p)}Y\right)\right]. \tag{36}$$

For convenient application of the Laplace inversion, Equation (36) is modified as

$$V(p,Y) = \mathcal{J}(p,Y) - \exp(-p)\mathcal{J}(p,Y)$$

$$+ \xi_7 G_r \mathcal{H}_1(p)\mathcal{H}_2(p)\left[\frac{\exp\left(-\sqrt{\frac{p\sigma_1}{\sigma_2+p}}Y\right)}{p} - \frac{\exp\left(-\sqrt{f_0(p)}Y\right)}{p}\right], \tag{37}$$

where

$$\xi_7 = \frac{\xi_2}{\xi_1}, \quad \xi_8 = \frac{\xi_3}{\xi_1(1+\lambda_1)}, \quad \xi_9 = \frac{\xi_3\xi_4\xi_5}{\xi_1(1+\lambda_1)}, \quad \xi_0 = \frac{\xi_1(1+\lambda_1)}{\xi_3},$$

$$\mathcal{H}_1(p) = \frac{1}{\sqrt{f_0(p)}-1}, \quad \mathcal{H}_2(p) = \frac{1}{(1+\lambda_2 p)f_4(p)-p}, \quad \sigma_1 = \frac{\xi_0}{\lambda_2},$$

$$f_4(p) = \frac{(P_r\xi_9)p}{p^\Omega(1-ap^{-\eta})^\psi}, \quad \mathcal{J}(p,Y) = \frac{\exp\left(-\sqrt{\frac{p\xi_0}{1+\lambda_2 p}}Y\right)}{p^2}, \quad \sigma_2 = \frac{1}{\lambda_2}. \tag{38}$$

Employing the Laplace inverse transformation on Equation (37) to transmute it back from the Laplace domain to the original domain, we obtained the following solution of the velocity field:

$$V(t,Y) = \mathcal{J}(t,Y) - \mathcal{J}(t-1,Y,)H(t-1,Y)$$

$$+ \xi_7 G_r \mathcal{H}_1(t) * \mathcal{H}_2(t) * \left[\Theta(t,Y,\sigma_1,\sigma_2) - \sum_{j=0}^{\infty} \frac{(-Y)^j (P_r\xi_4\xi_5)^{\frac{j}{2}}}{j!} E^{\frac{j\psi}{2}}_{\eta,1+\frac{j(1-\Omega)}{2}}(at^\eta)\right], \tag{39}$$

where

$$\mathcal{J}(t,Y) = \frac{\xi_0}{\lambda_2} \int\limits_0^\infty \int\limits_0^t \exp\left(\frac{u + r(\xi_0)}{\lambda_2}\right) \mathrm{erfc}\left(\frac{Y}{2\sqrt{r}}\right) I_0\left(\frac{2}{\lambda_2}\sqrt{\xi_0(ur)}\right) du\, dr,$$

$$\mathcal{H}_1(t) = \sum_{j=1}^\infty \frac{(-P_r\xi_4\xi_5)^j}{j!} t^{(j-1)\Omega-1} E_{\eta,(j-1)\Omega}^{j\psi}(at^\eta) \int\limits_0^\infty \zeta^j u(\zeta)d\zeta + \delta(t)\int\limits_0^\infty u(\zeta)d\zeta,$$

$$\mathcal{H}_2(t) = -\sum_{j=0}^\infty \sum_{k=0}^\infty \frac{(P_r\xi_9)^j \lambda_2^k j!}{k!(j-k)!} t^{(j\Omega-k)} E_{\eta,j\Omega-k+1}^{j\psi}(at^\eta),$$

$$\Theta(t,Y,\sigma_1,\sigma_2) = 1 - \frac{2\sigma_1}{\pi}\int\limits_0^\infty \frac{\sin(Ys)}{s(\sigma_1+s^2)}\exp\left(\frac{-\sigma_2 s^2 t}{\sigma_1+s^2}\right)ds. \tag{40}$$

3.4. Solution for Classical Velocity Distribution

The solution of the flow equation for the case of classical framework is evaluated as

$$V(p,Y) = \mathcal{J}(p,Y) - \exp(-p)\mathcal{J}(p,Y)$$
$$+ \frac{(\xi_7 G_r)\mathcal{H}_3(p)}{(\xi_9 P_r)\lambda_2\left[\frac{1}{\lambda_2} + p - \frac{1}{(\xi_9 P_r)\lambda_2}\right]}\left[\frac{\exp\left(-\sqrt{\frac{p\sigma_1}{\sigma_2+p}}Y\right)}{p} - \frac{\exp\left(-\sqrt{p(\xi_4\xi_5)P_r}Y\right)}{p}\right]. \tag{41}$$

By applying the Laplace inverse transform on Equation (41), the following version of the flow function is derived in the primary domain:

$$V(t,Y) = \mathcal{J}(t,Y) - \mathcal{J}(t-1,Y)H(t-1,Y)$$
$$+ \frac{\xi_7 G_r}{(\xi_9 P_r)\lambda_2}\mathcal{H}_3(t) * \exp\left(\frac{1-\xi_9 P_r}{\lambda_2(\xi_9 P_r)}t\right) * \left[\Theta(t,Y,\sigma_1,\sigma_2) - \mathrm{erfc}\left(\frac{\sqrt{(\xi_4\xi_5)P_r}Y}{2\sqrt{t}}\right)\right], \tag{42}$$

where $\mathcal{H}_3(p)$ and $\mathcal{H}_3(t)$ are specified as

$$\mathcal{H}_3(p) = \frac{1}{p\left(\sqrt{p(\xi_4\xi_5)P_r}-1\right)}, \quad \mathcal{H}_3(t) = \left[\mathrm{erf}\left(\frac{\sqrt{t}}{\sqrt{(\xi_4\xi_5)P_r}}\right)+1\right]\exp\left(\frac{t}{(\xi_4\xi_5)P_r}\right) - 1. \tag{43}$$

3.5. Pertinent Physical Quantities

The skin friction coefficient and Nusselt number are two important mathematical quantities to study shear stress and heat transfer phenomena. For the current model, the expressions for these quantities are provided as

$$Nu = \frac{q^*}{h\top_\infty}, \qquad C_f = \frac{\tau^*}{\widehat{\mu}_{\mathrm{VPO}}\left(\frac{hV_0}{\widehat{\mathcal{K}}_{\mathrm{VPO}}}\right)}, \tag{44}$$

where the relations for q^* and τ^* are supplied as

$$q^* = -\widehat{\mathcal{K}}_{nf} \left.\frac{\partial \top^*(t^*, Y^*)}{\partial Y^*}\right|_{Y^*=0}, \qquad \tau^* = \frac{\widehat{\mu}_{nf}}{1+\lambda_1}\left(1+\lambda_0 \frac{\partial}{\partial t^*}\right) \left.\frac{\partial V^*(t^*, Y^*)}{\partial Y^*}\right|_{Y^*=0}. \qquad (45)$$

On solving Equations (44) and (45) and simplifying, we acquired the following unit-independent expressions for the Nusselt number and skin friction coefficient:

$$Nu = -\xi_5 \left.\frac{\partial \top(t, Y)}{\partial Y}\right|_{Y=0}, \qquad C_f = \frac{\xi_3}{1+\lambda_1}\left(1+\lambda_2 \frac{\partial}{\partial t}\right) \left.\frac{\partial V(t, Y)}{\partial Y}\right|_{Y=0}. \qquad (46)$$

4. Results and Discussion

This study focuses on the development of a mathematical model to examine how vacuum pump oil's heat-transporting characteristics are affected by the distribution of aluminum alloy nanoparticles. To understand the relevance of the shape component, the chosen nanoparticles are assumed to have multiple shapes (blade, platelet, cylinder, and brick). This investigation is performed by bringing the Prabhakar fractional operator into play for the establishment of a generalized model. This model is comprised of coupled equations that deal with the formation and variation of thermal and velocity boundary layers. The development of flow is aided by a ramped flow function, whereas heat transfer through an infinitely long surface begins as a result of the Newtonian heating process. Corresponding to non-uniform conditions, the analytic treatment of generalized mathematical systems for the evaluation of analytic solutions becomes exceedingly complex, and in such cases, numerical or semi-analytic solutions are favored. However, a special effort to attain exact solutions is made in this work, and the constituted model is successfully solved in both conventional and fractional environments. The motive of establishing exact solutions is achieved by executing the Laplace transform on basic and fractional equations. This section is dedicated to a comprehensive interpretation of the behavior of the principal quantities with the assistance of tabular data and graphical illustrations. These quantities include velocity function, Nusselt number, energy function, and shear stress. For a thorough observation of the transient effects, graphs and tables are developed for multiple time values. To highlight the significance of the following fractional approaches for modeling purposes, a comparison of the velocity and energy fields is drawn for the conventional and fractional models. This section also discusses how alteration of the associated parameters attenuates or expands the thickness of the boundary layers. Moreover, some comparative illustrations and tables are presented to examine the effects of four different shapes of nanoparticles on the properties of the host fluid. The computational values for thermal and physical attributes of vacuum pump oil and nanoparticles are imparted in Table 3.

Table 3. Computational values for thermal and physical characteristics of aluminum alloy nanoparticles and vacuum pump oil [45,46].

Properties	Units	Host Fluid	Nanoparticles
		Vacuum Pump Oil	Aluminum Alloy
$\widehat{\mathcal{C}}_p$	$\mathrm{J\,kg^{-1}K^{-1}}$	2320	960
$\widehat{\rho}$	$\mathrm{kg\,\,m^{-3}}$	870	2810
$\widehat{\mathcal{K}}$	$\mathrm{W\,\,m^{-1}K^{-1}}$	0.13	173

The overall influence of the fractional parameters (ψ, η, and Ω) on velocity and energy distributions is investigated in Figures 2a,b and 3a,b. These graphs are developed to accommodate a wide range of larger and smaller time magnitudes in order to provide thorough insight. For rising alterations of fractional parameters, the graph of the temperature field is shown to express a declining pattern for larger time values, while the choice of a minimum

magnitude of time causes an upsurge in the value of the energy function. The behavior of the velocity graph subject to modification of fractional parameters is no different from that of the temperature curve. Since the ramped condition for the flow function is employed, therefore, when $t \leq 1$, the starting point of the flow function is separate for different values of time. However, when $t > 1$, the curve of the flow function initiates from the same point for two dissimilar values of time. This is how the application of a ramped velocity condition offers better control over the flow during complex and flow-sensitive operations. The kernel of a fractional operator is the key factor for particular behaviors of thermal and velocity functions. For the current study, this dual behavior of the principle functions for higher and smaller time values is attributed to the multiparametric kernel. The memory-retaining characteristic of the fractional derivative allows it to remember the history of the involved functions at prior steps and apply that information to subsequent steps. For a greater comprehension of flow and thermal patterns and to emphasize the contribution of the considered conditions, three-dimensional (3D) illustrations of energy and velocity functions are, respectively, provided in Figure 4a,b. According to Figure 4a, an elevation in the thermal profile takes place at the solid–nanofluid interface, corresponding to a rise in time values, which is unusual since it does not occur when an isothermal condition is considered. Meanwhile, the 3D illustration of the flow field is composed of two regions. The gray region is associated with the time-independent part of the velocity constraint; therefore, the flow profile in this region starts from the same point at the boundary for all values of time. On the other end, the flow function and time have the same values at the solid–nanofluid interface in the red region because the flow patterns in this region correspond to the part of the velocity condition that depends on time inputs. After considering the combined impacts of all the fractional parameters, it is worth investigating the conduct of velocity and thermal profiles for the adjustment of an individual fractional parameter. In this regard, Figures 5 and 6 are prepared for multiple values of η and t. It can be seen that both profiles exhibit the same prior behavior, which is a drop for a higher value of time and an elevation for smaller time inputs. Hence, it is concluded that both individual parameter adjustments and a combination of these parameter variations have the same effects on thermal and velocity profiles. These findings indicate that the fractional model is highly efficient as compared to a conventional model since it offers more freedom to manage flow and energy fields. In addition to this, it is quite clear that differences in thermal profiles because of the modification of fractional parameters are more explicit for greater time inputs. Moreover, when the velocity patterns for variable and constant parts of the ramped velocity relation are compared, it is perceived that the graph of the velocity field is always superior for the case of a constant velocity function at the solid–nanofluid interface. Applying such conditions is useful to successfully achieve improved control on the flow because, in the presence of a ramped velocity function, time variations have a substantial impact on the formation of flow patterns at the boundary.
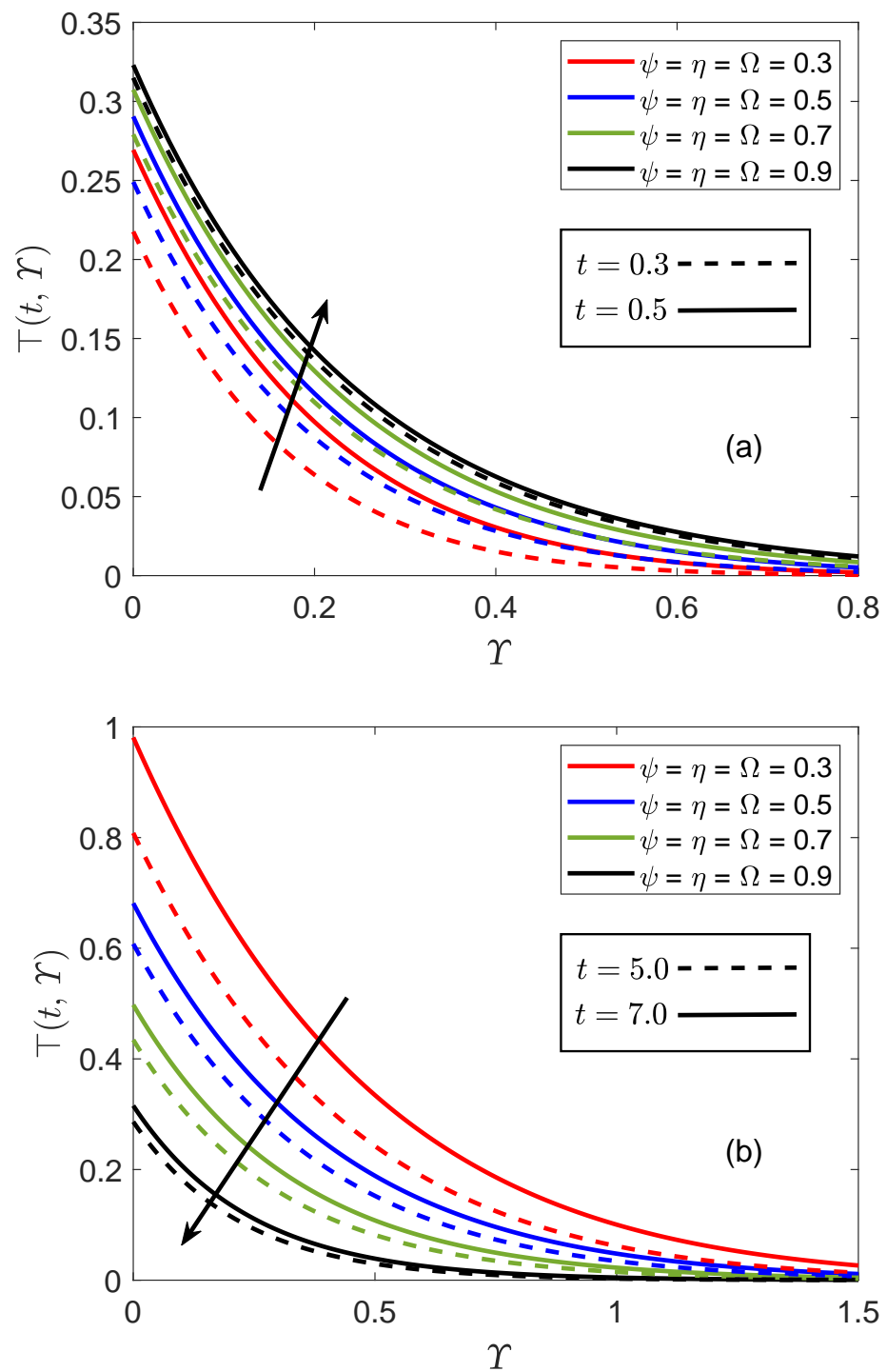
Figure 2. (**a**) Thermal profile corresponding to variation of ψ, η, and Ω for smaller time inputs. (**b**) Thermal profile corresponding to variation of ψ, η, and Ω for larger time inputs.
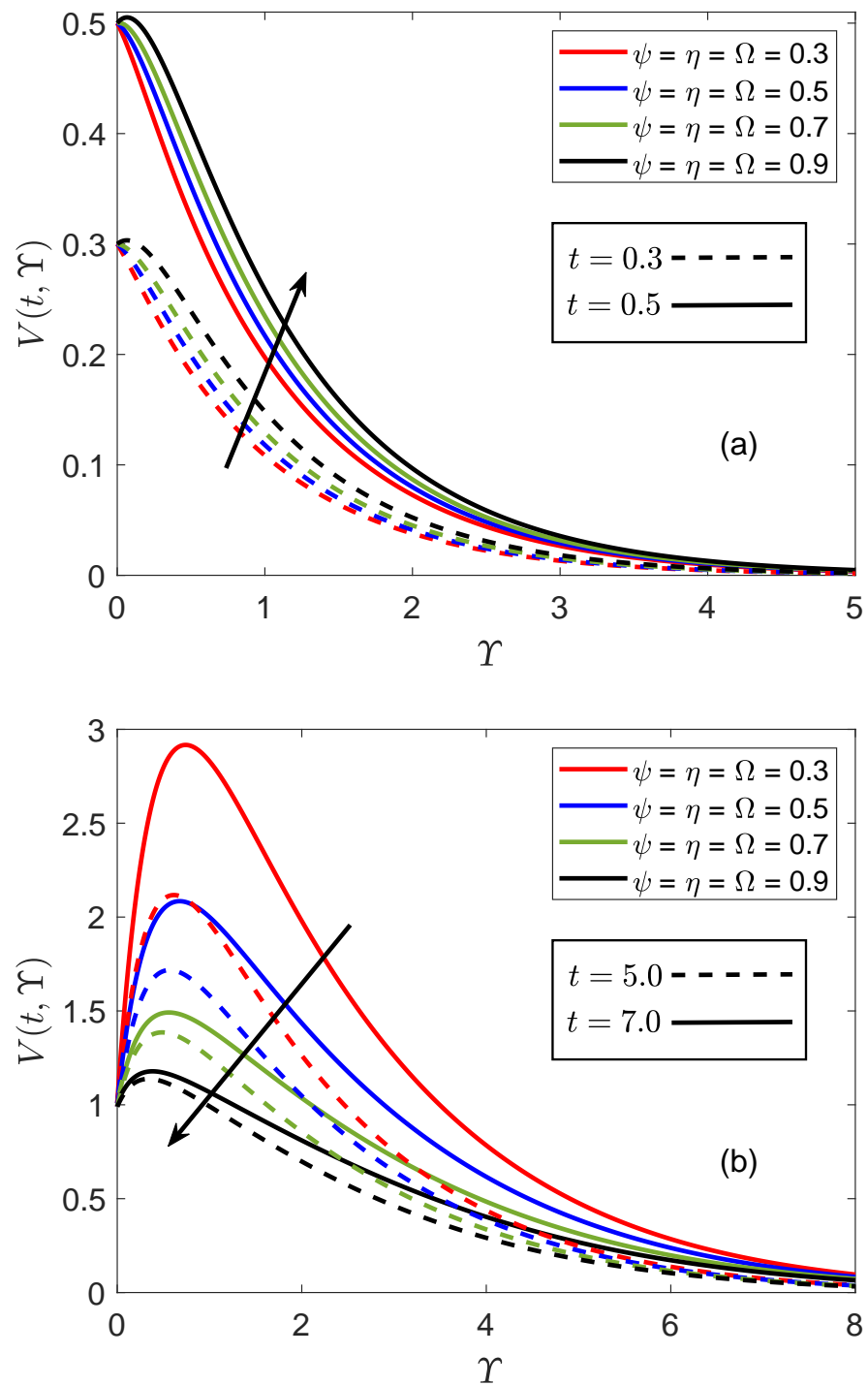
Figure 3. (**a**) Flow profile corresponding to variation of ψ, η, and Ω for smaller time inputs. (**b**) Flow profile corresponding to variation of ψ, η, and Ω for larger time inputs.
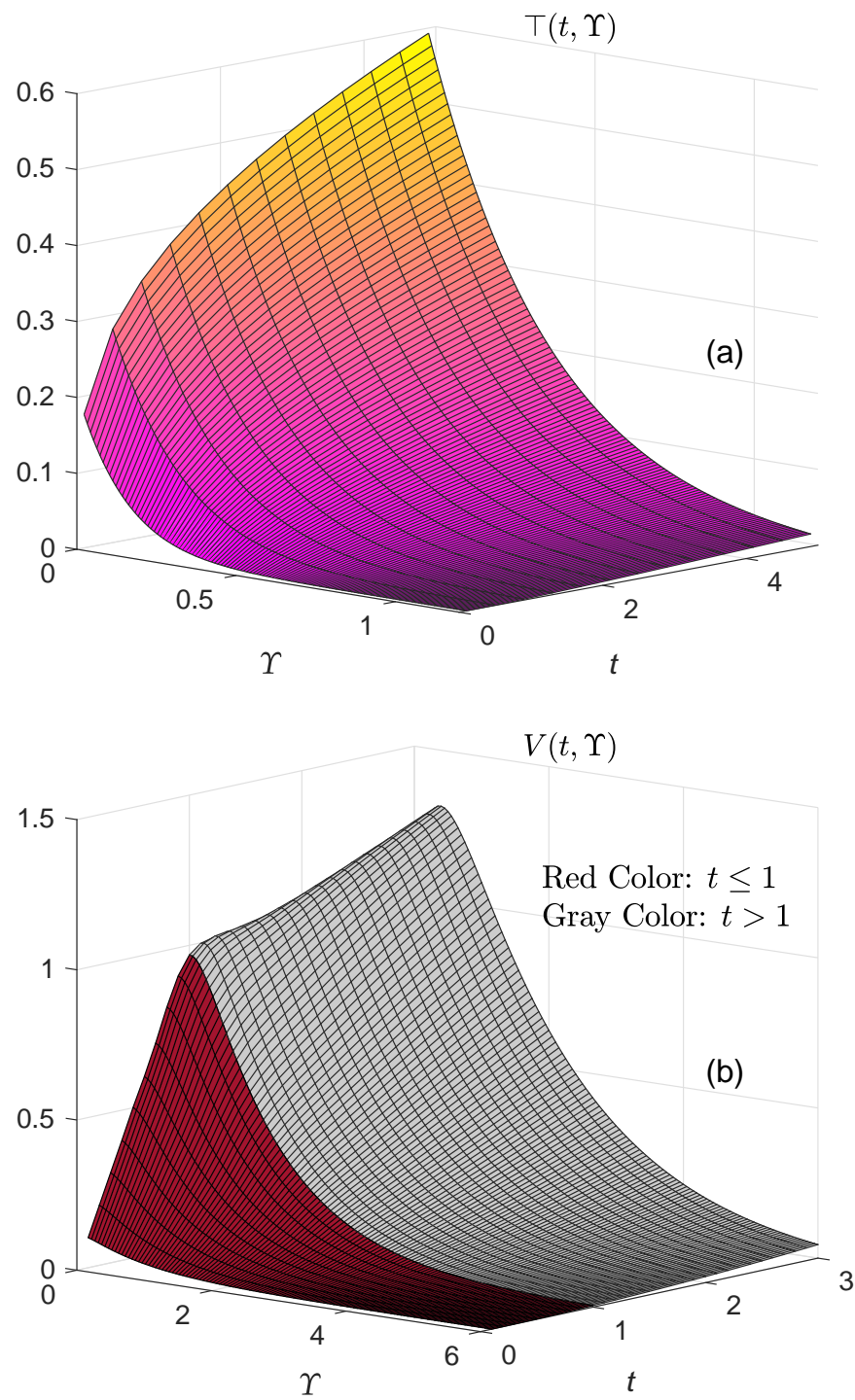
Figure 4. (**a**) Three-dimensional illustration of thermal profile. (**b**) Three-dimensional illustration of flow profile.
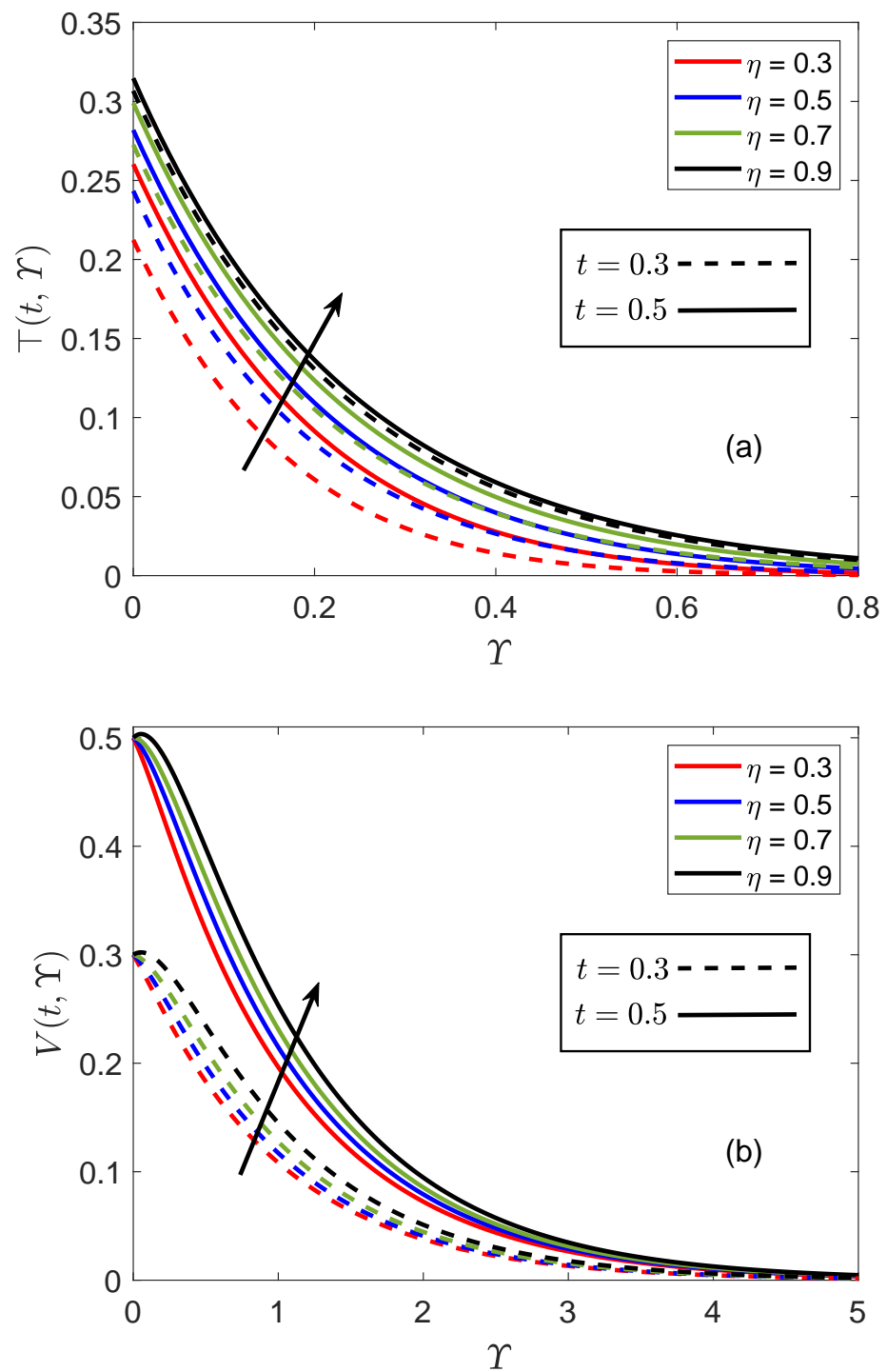
Figure 5. (**a**) Thermal patterns corresponding to change in η for smaller time inputs. (**b**) Flow patterns corresponding to change in η for smaller time inputs.
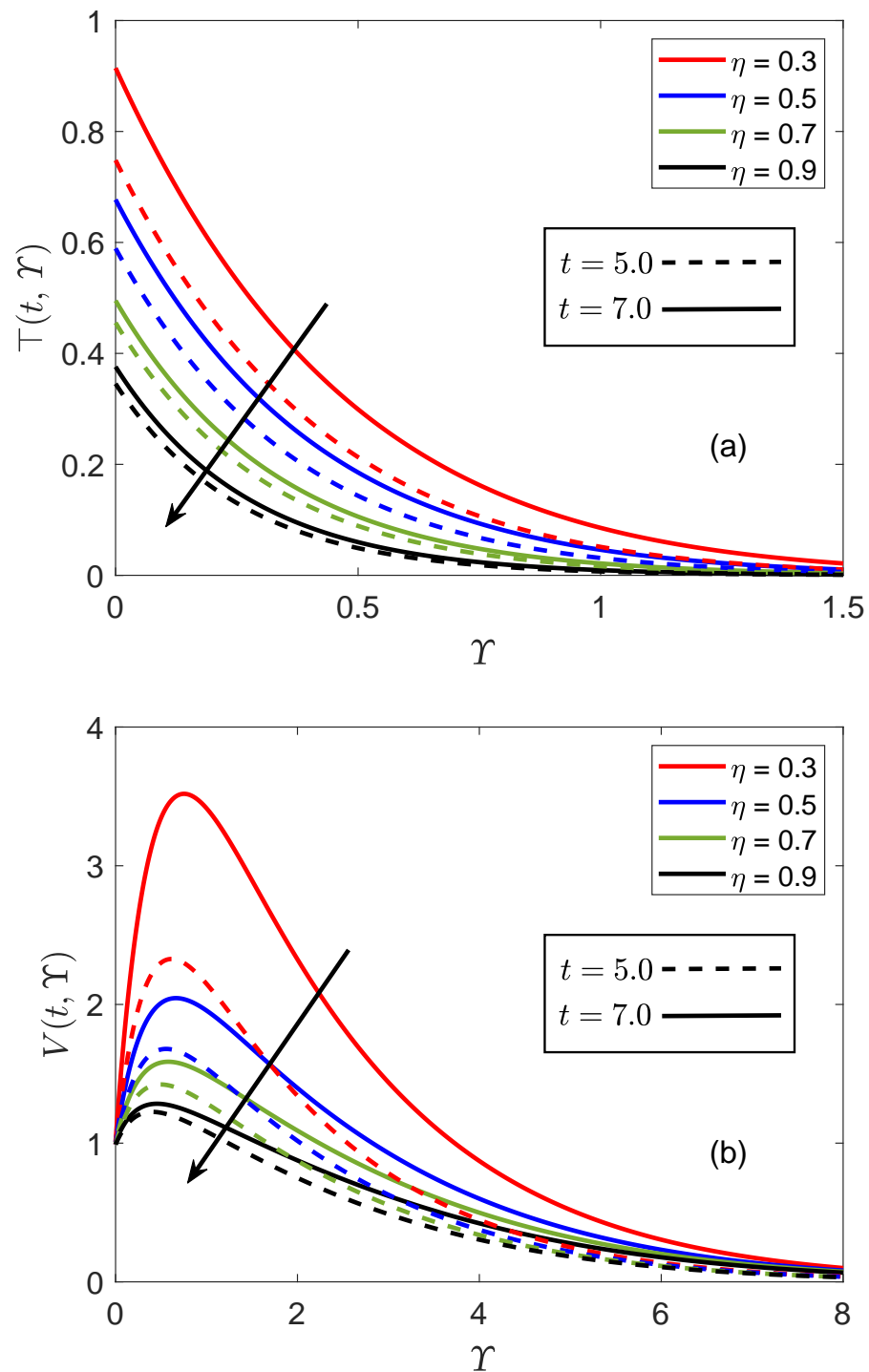
Figure 6. (**a**) Thermal patterns corresponding to change in η for larger time inputs. (**b**) Flow patterns corresponding to change in η for larger time inputs.

There are several key advantages of using fractional models for the explanation of flow and thermal distributions that cannot be obtained by applying classical governing models. For instance, the memory-retaining characteristics of a fractional model allow it to remember the history of the involved functions at prior steps and apply that information to subsequent steps. In this way, more generalized solutions are developed, which can be modified with the adjustment of the fractional parameter. The fractional model formulated through a particular fractional derivative effectively captures all viscous, material, and

elastic features of fluids. As compared to conventional models, fractional models provide better control over flow and heat transfer mechanisms, which is crucial for ultrasensitive processes. The fractional operators adequately elucidate crossover behaviors and rheological attributes because of their self-similar properties. In addition, an accurate accordance between the experimental reports and the theoretic results produced through fractional systems can be established by appropriately modifying the fractional parameters. The precision and reliability of the results obtained in fractional frameworks are relatively higher than those acquired in classical settings. Thus, it can be concluded that fractional models provide a better and more accurate description of the problems being modeled.

Figures 7 and 8 are constructed to highlight the thermal and flow behavior of vacuum pump oil under the effects of different shapes of aluminum alloy nanoparticles. These figures delineate that the thermal function is enhanced to its optimum capacity when alloy particles of blade-like shapes are distributed in the host fluid. Contrary to that, the suspension of brick-shaped nanoparticles produces the least improvement in thermal function. The trend exhibited by the thermal profile for the distinct shapes of nanoparticles is mainly influenced by the sphericity of these nanoparticles. The fraction of a sphere's surface area to that of actual particles with equivalent volumes is referred to as sphericity. To deal with the shape-dependent thermal conductivity of nanoparticles, the Hamilton and Crosser relation [40] is utilized for this study. In this relation, the shape component α encounters the sphericity (Ψ) of nanoparticles as $\alpha = 3/\Psi$. The direct correlation of thermal conductivity and viscosity may also be ascribed for the present behavior. It is conspicuous from the superior thermal curves of platelet- and blade-shaped nanoparticles in Figures 7a and 8a as particles of these shapes possess higher thermal conductivities as equated to those nanoparticles, which have brick- and cylinder-like shapes. Meanwhile, a different pattern of flow field subject to changes of nanoparticles' shape is witnessed in Figures 7b and 8b. It is noted that adding platelet-shaped particles to vacuum pump oil significantly decelerates the motion of the consequent nanofluid. On the opposite end, the highest flow profile is associated with blade-shaped nanoparticles. The trend followed by the velocity function for these shapes is the same for larger and lower values of time; however, the differences in curves are more clear for the former case. The principal quantities due to which the velocity function of nanofluid specifies a particular pattern of the flow profile are shape constants κ_1 and κ_2. Depending on how nanoparticles are shaped, these two parameters either maximize or diminish the viscosity of the nanofluid. Keeping a view of Figures 7b and 8b, it can be remarked that when nanoparticles of a platelet-shape are dispensed in vacuum pump oil, the resulting nanofluid becomes highly viscous. Since the tendency of cylinder-, brick-, and blade-shaped particles to make the host fluid viscous is comparatively lower than that of platelet-shaped particles, the velocity curves associated with these particles are higher.

Figures 9 and 10 serve as support for the investigation into the effects of altering the loading range (φ) of nanoparticles in the host fluid on velocity and thermal distributions. The profiles of thermal and flow fields for three different φ inputs are portrayed in these figures. Figures 9a and 10a demonstrate an elevation in the profile of the thermal field as a consequence of a positive alteration of φ. It is also identified that the temperature distribution communicates the lowest profile for the case of pure vacuum pump oil. This difference in thermal profiles highlights the weak tendency of vacuum pump oil to facilitate heat transfer. However, when alloy particles are added to it, their strong thermal features boost the heat-transporting ability of vacuum pump oil. Due to this advancement in thermal properties, the resulting nanofluid is capable of absorbing more heat at the boundary; therefore, the heat transfer process takes place at an improved rate at the interface. Consequently, higher temperature profiles, indicating a significant rise in energy function, are observed in Figures 9a and 10a. Contrary to that, the flow profile of the nanofluid shows a decreasing behavior when the proportion of particles in the host fluid is magnified, as depicted in Figures 9b and 10b. The corresponding figures further reveal that the flow function of pure vacuum pump oil possesses greater values than that of the consequent nanofluid. The viscosity of the host fluid keeps enhancing as

long as the concentration of nanoparticles in the fluid continues to improve, which is one of the fundamental features of nanoparticles in the physical sense. For the maximum loading range of alloy nanoparticles, the under-observation nanofluid is more viscous in nature than regular vacuum pump oil; therefore, a decline in flow patterns can be specified from the respective figures. The purpose of producing Figure 11a,b is to examine the participation of the relaxation parameter (λ_1) in the development of flow patterns. The impacts of λ_1 on the velocity distribution are fascinating because the graphs of the flow function for smaller and higher values of t are a little different from each other. For $t = 0.3$ and $t = 0.5$, the velocity of the nanofluid diminishes in consequence to the augmenting variation of λ_1. Whereas, for the case of higher time inputs, a dual behavior of the flow function is witnessed against the changing values of λ_1. In the physical sense, when the influence of parameter λ_1 becomes dominant, the thickness of the flow boundary layer extends. The parameter λ_1 represents the elasticity and viscous nature of the nanofluid, thus, it is obvious that the nanofluid will have stronger viscous and elastic properties for higher values of λ_1. As a consequence, the flow occurs at a slower rate. However, for a longer duration, this effect comes into existence comparatively later than it appears in the case of lower time values. Finally, at the far end, the flow function of the presented nanofluid obtains a zero value as the influence of acting forces becomes insignificant.
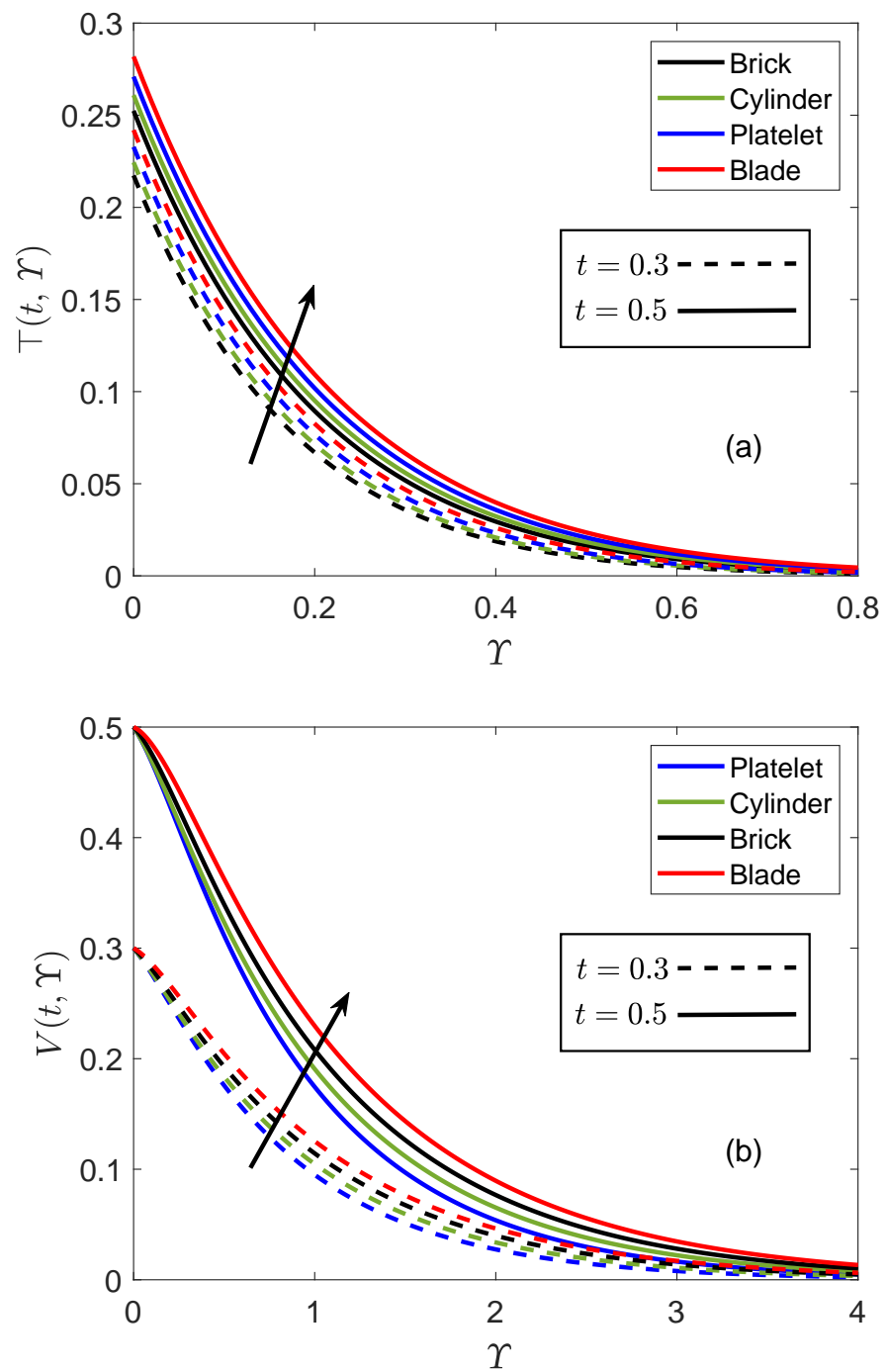
Figure 7. (**a**) Thermal patterns for different shapes of nanoparticles and smaller time inputs. (**b**) Flow patterns for different shapes of nanoparticles and smaller time inputs.
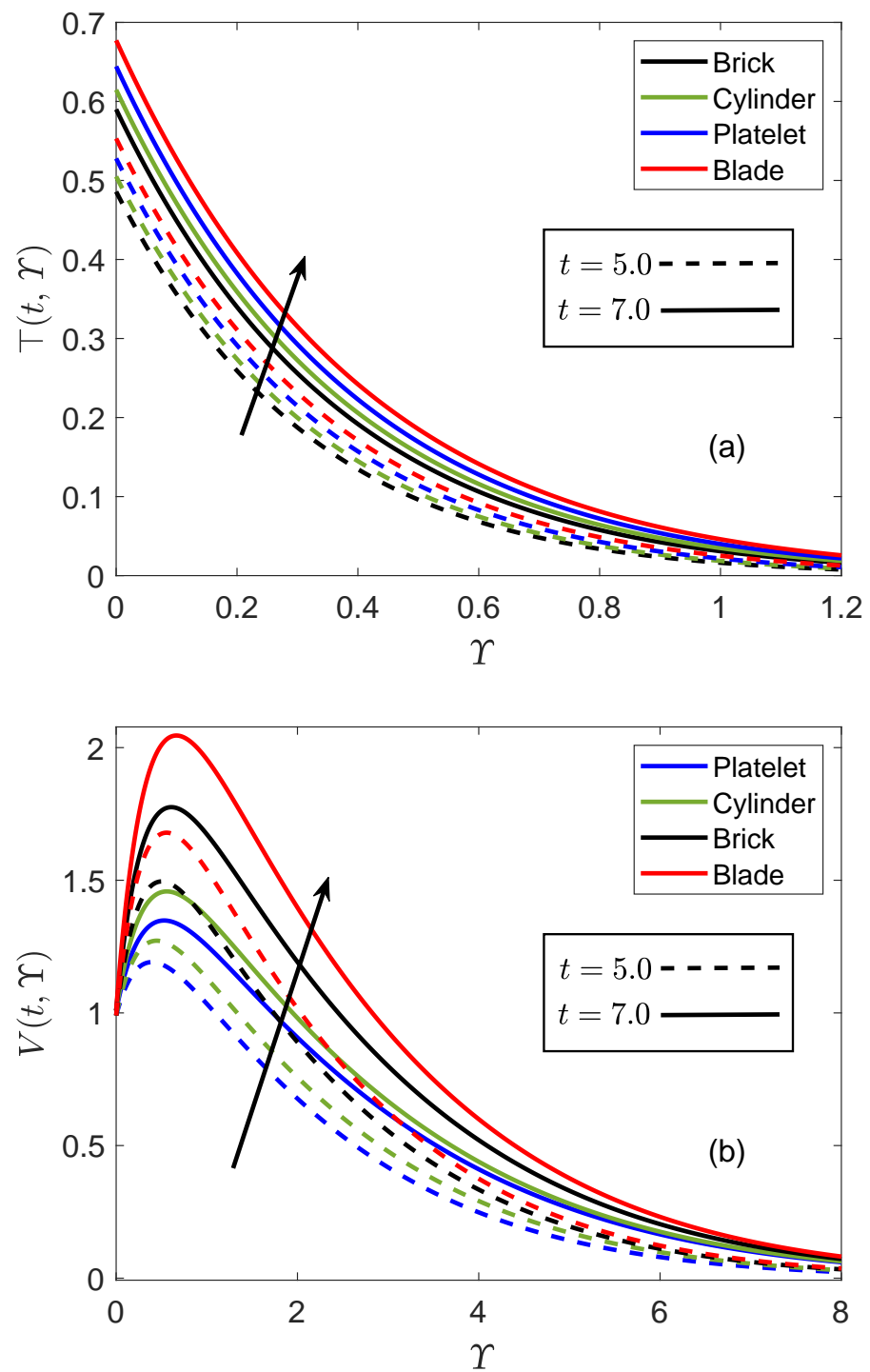
Figure 8. (**a**) Thermal patterns for different shapes of nanoparticles and larger time inputs. (**b**) Flow patterns for different shapes of nanoparticles and larger time inputs.
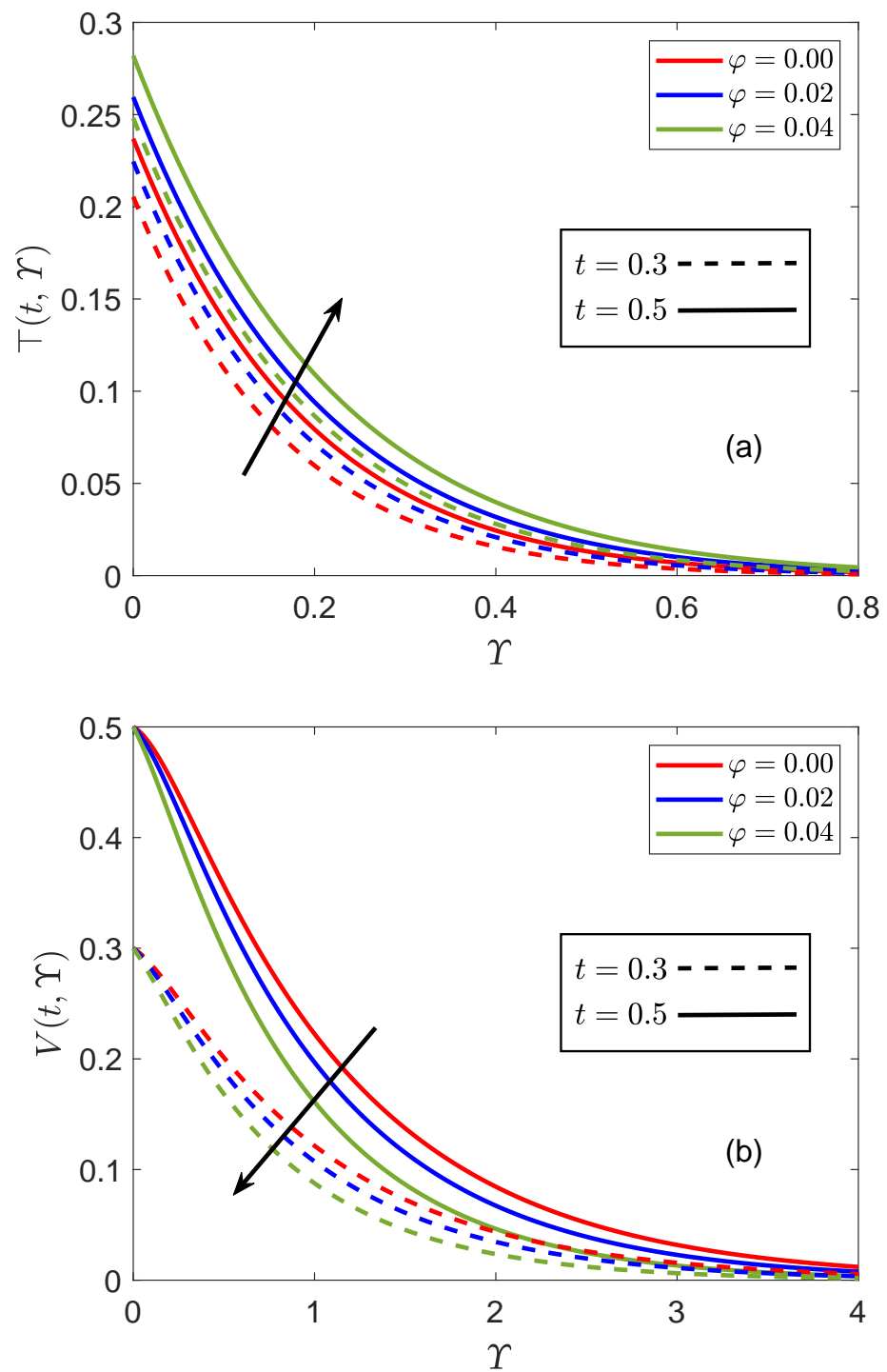
Figure 9. (**a**) Thermal patterns corresponding to variations of φ for smaller time inputs. (**b**) Flow patterns corresponding to variations of φ for smaller time inputs.
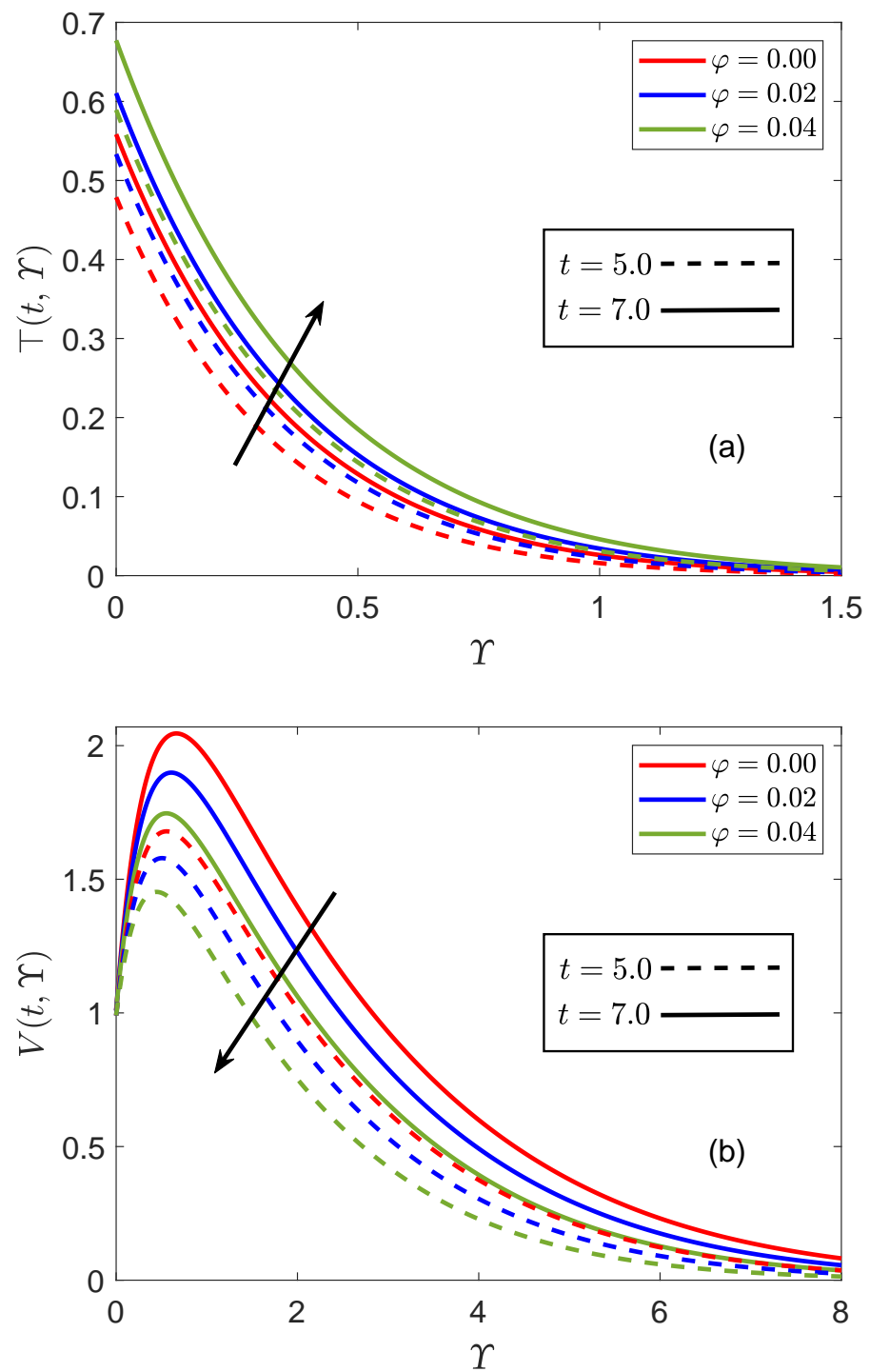
Figure 10. (**a**) Thermal patterns corresponding to variations of φ for larger time inputs. (**b**) Flow patterns corresponding to variations of φ for larger time inputs.
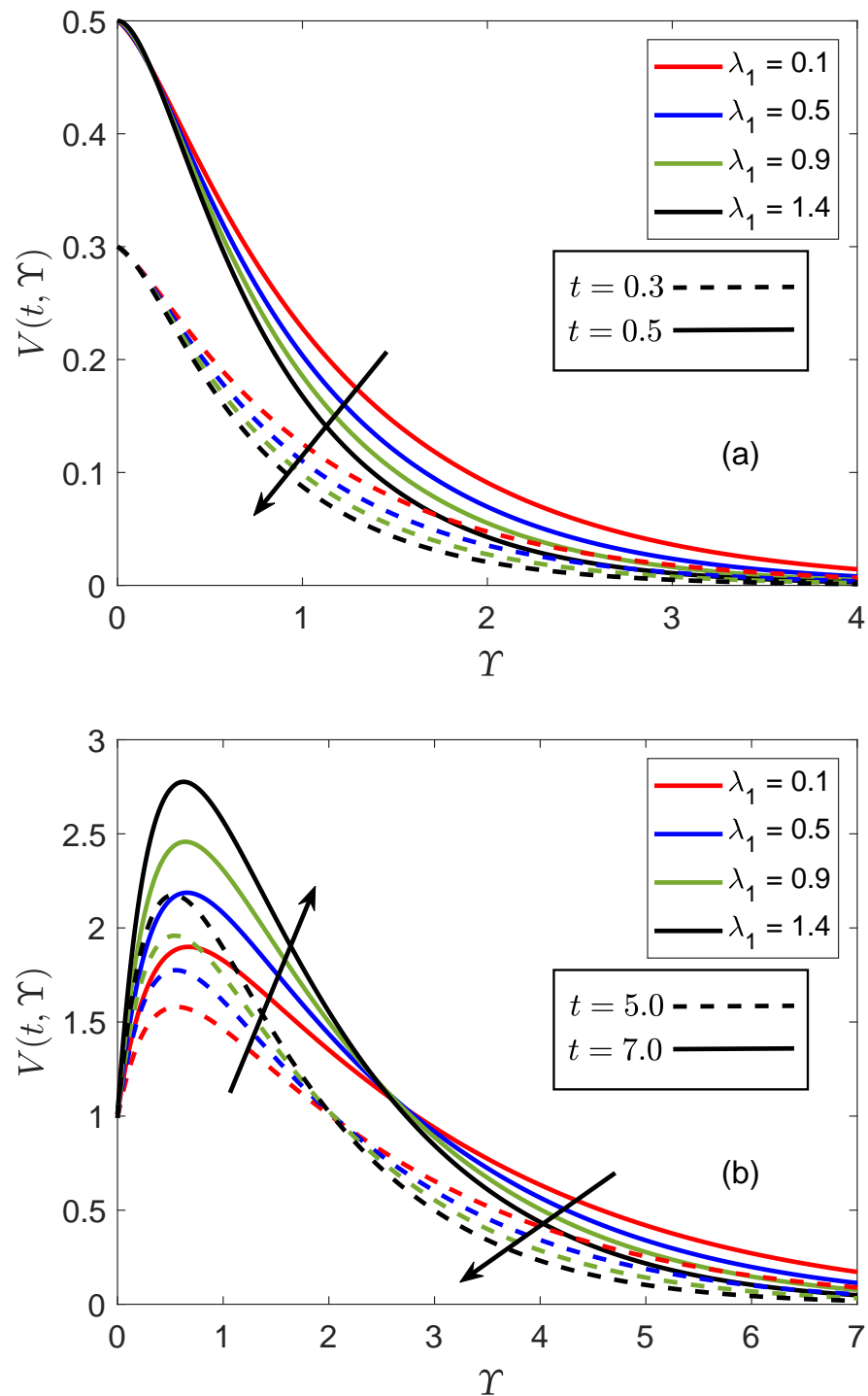
Figure 11. (**a**) Flow patterns corresponding to variations of λ_1 for smaller time inputs. (**b**) Flow patterns corresponding to variations of λ_1 for larger time inputs.

The forces resisting or favoring the motion of a nanofluid are primarily distributed into two categories based on their behavior. The first category of forces, which is important for the expedition of flow, includes the buoyancy force. On the other hand, viscous forces belong to the second type and produce substantial opposition to the motion of nanofluids and act against the direction of flow. To properly comprehend such practical operations that involve fluid transportation and heat transfer, accurate forecasting of the aforementioned forces is absolutely indispensable. These forces can be appropriately estimated by the

dint of a single quantity titled the Grashof number (G_r) for those physical phenomena where the development of flow is significantly attributed to natural convection. When it comes to discuss the Grashof number from the mathematical point of view, it is a proportion of viscous and buoyancy effects such that it maintains an inverse relation with the former and a direct relation with the latter. An amelioration in the magnitude of G_r depicts that the boundary has received additional heat, which boosts the temperature of the bounding surface. This augmentation leads to several physical consequences that take part in controlling the flow performance of the nanofluid. In particular, the neighboring layers of the presented fluid adjacent to the fluid–solid interface exhibit peculiar weight disparities. Aside from that, depletion in the dominance of internal friction is also accredited to this enhanced temperature. Considering the dominant influences of G_r on the flow mechanism, Figure 12a,b are composed to scrutinize the repercussions of varying G_r values on the flow conduct of the considered nanofluid. The elevation of the velocity profiles in the respective figures by virtue of G_r increment signifies that the flow becomes accelerated in this case. From the physical perspective, additional heating causes a density shift in the flow region, which eventuates the development of a convectional current. Furthermore, the convectional current produces a buoyant force and also serves to boost its intensity, making the control of viscous effects on the flow minimal. As a consequence, the nanofluid encounters insignificant resistance during the flow, due to which its velocity is expedited, and the flow function specifies an elevated profile, as displayed in Figure 12a,b.

Figure 13a,b are imparted to examine how the Jeffery parameter (λ_2) affects the flow patterns. To thoroughly evaluate the ramifications of λ_2 modification, these figures are created for a wide range of time inputs. It is found that λ_2 and the flow function are directly related for lower time inputs. Meanwhile, for a longer time duration, the behavior of the flow function is dual, i.e., it reduces initially, but later on, it increases. On comparison, it can be perceived that the conduct of the flow profiles for λ_1 and λ_2 are quite contrasting to each other. Equation (8) provides mathematical support for this conduct of the flow profile because λ_1 and λ_2 share an inverse relationship with the velocity function in this equation. The aim of Figures 14 and 15 is to compare the solutions of energy and velocity functions for conventional and fractional mathematical systems. According to Figure 14a, when t has lower values, the thermal profile obtained by virtue of the conventional model is lower than the thermal profile of the generalized model. Contrary to that, for the case of larger t inputs, the classical temperature function produces a higher thermal profile as portrayed in Figure 14b. In a similar manner, Figure 15a reveals that the flow curve associated with the generalized velocity field is superior to the flow curve acquired via the classical system. The aforementioned observation is for lower inputs of t; however, a reverse pattern is identified when greater values of time are considered. In this case, the fractional model provides a lower profile of velocity distribution, as demonstrated in Figure 15b. It is also evaluated from Figure 15a,b that in comparison to a ramped boundary velocity condition, the flow profile of the nanofluid is substantially higher for uniform movement of the bounding surface. Furthermore, the thickness of the momentum boundary layer is also greater in the case of a constant boundary flow function. These results accentuate that the aim of having appropriate control over the flow mechanism can be achieved through the utilization of ramped velocity conditions.

Figure 12. (**a**) Flow patterns corresponding to variations of G_r for smaller time inputs. (**b**) Flow patterns corresponding to variations of G_r for larger time inputs.

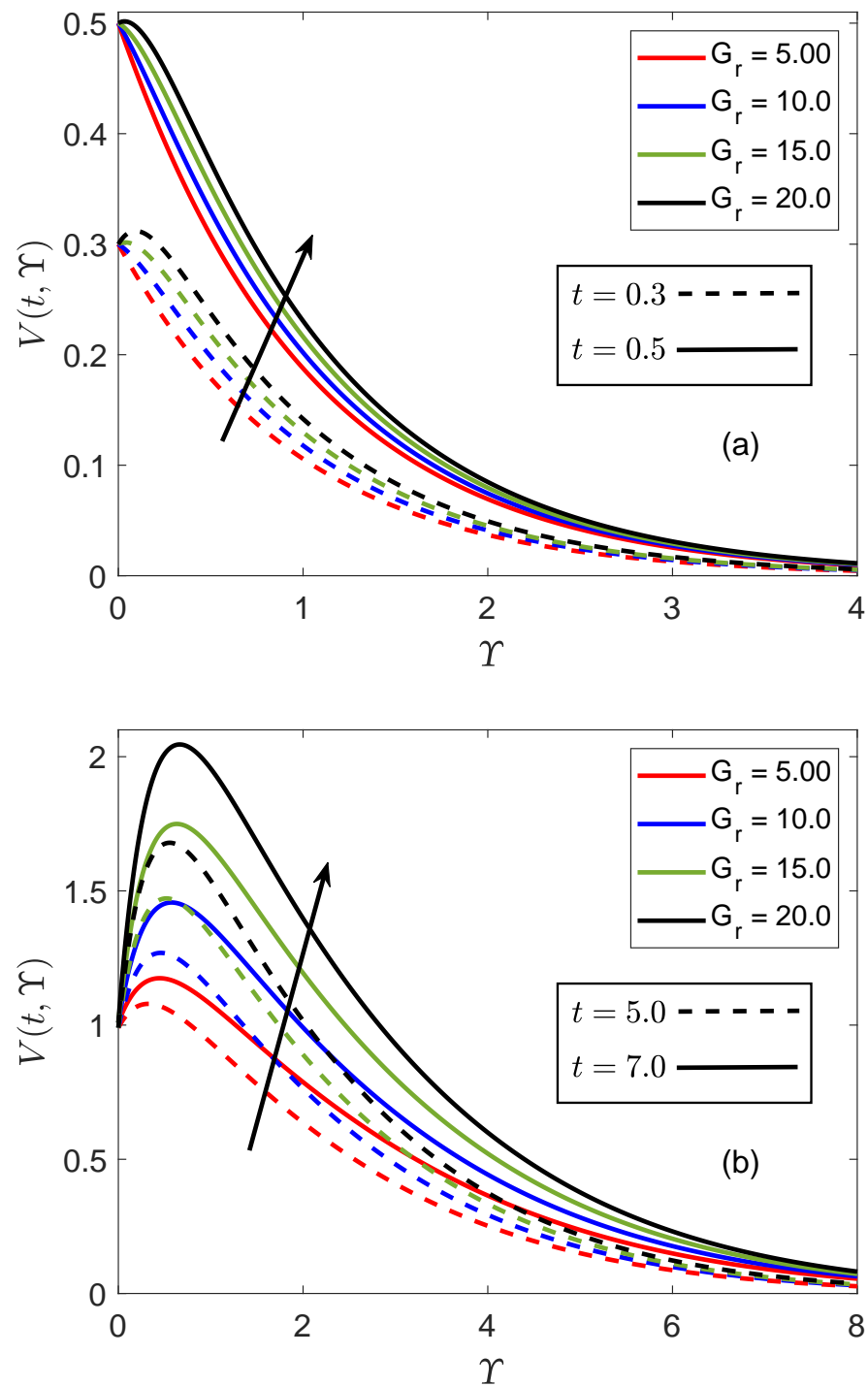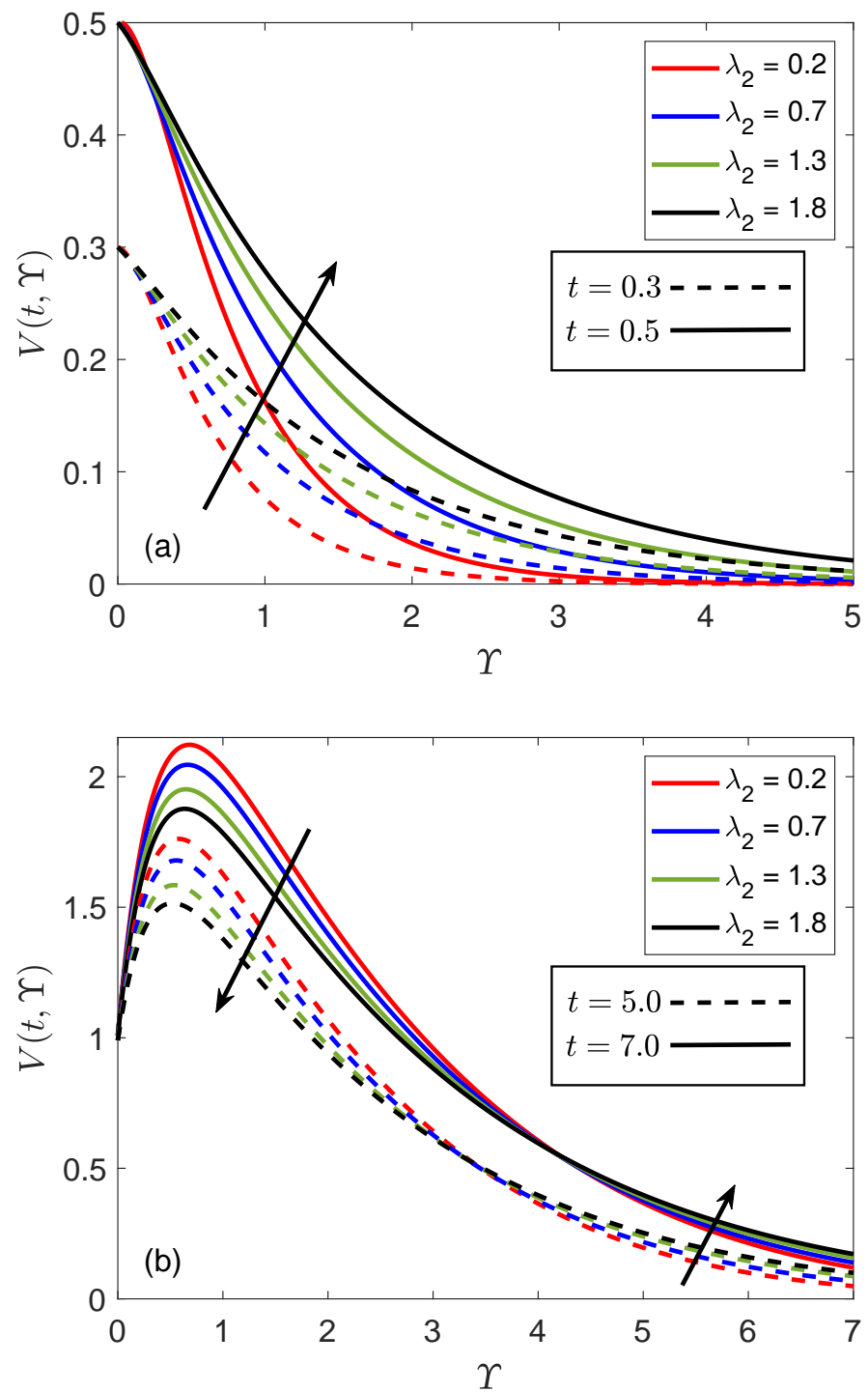**Figure 13.** (**a**) Flow patterns corresponding to variations of λ_2 for smaller time inputs. (**b**) Flow patterns corresponding to variations of λ_2 for larger time inputs.

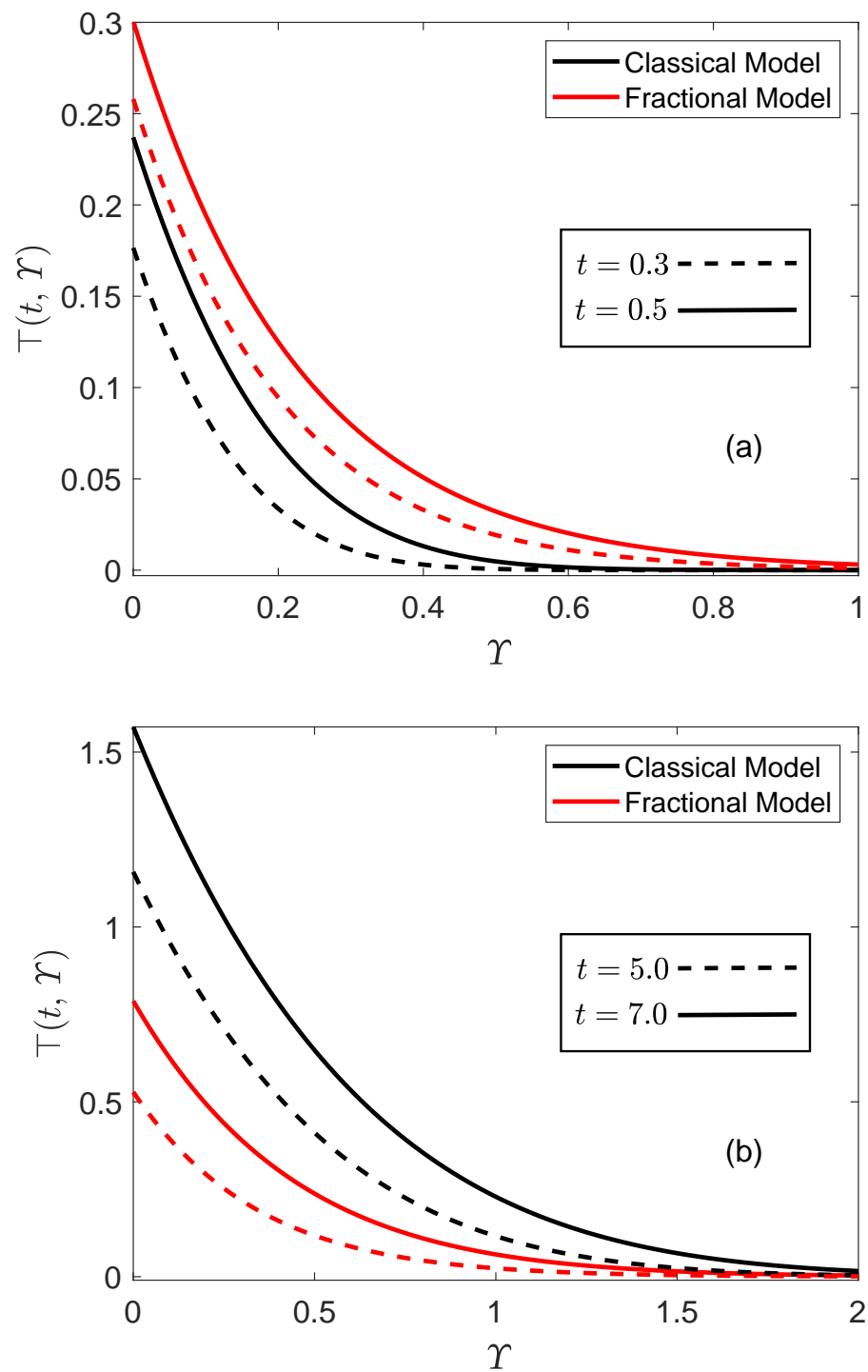**Figure 14.** (**a**) Thermal profile corresponding to fractional and classical cases for smaller time inputs. (**b**) Thermal profile corresponding to fractional and classical cases for larger time inputs.
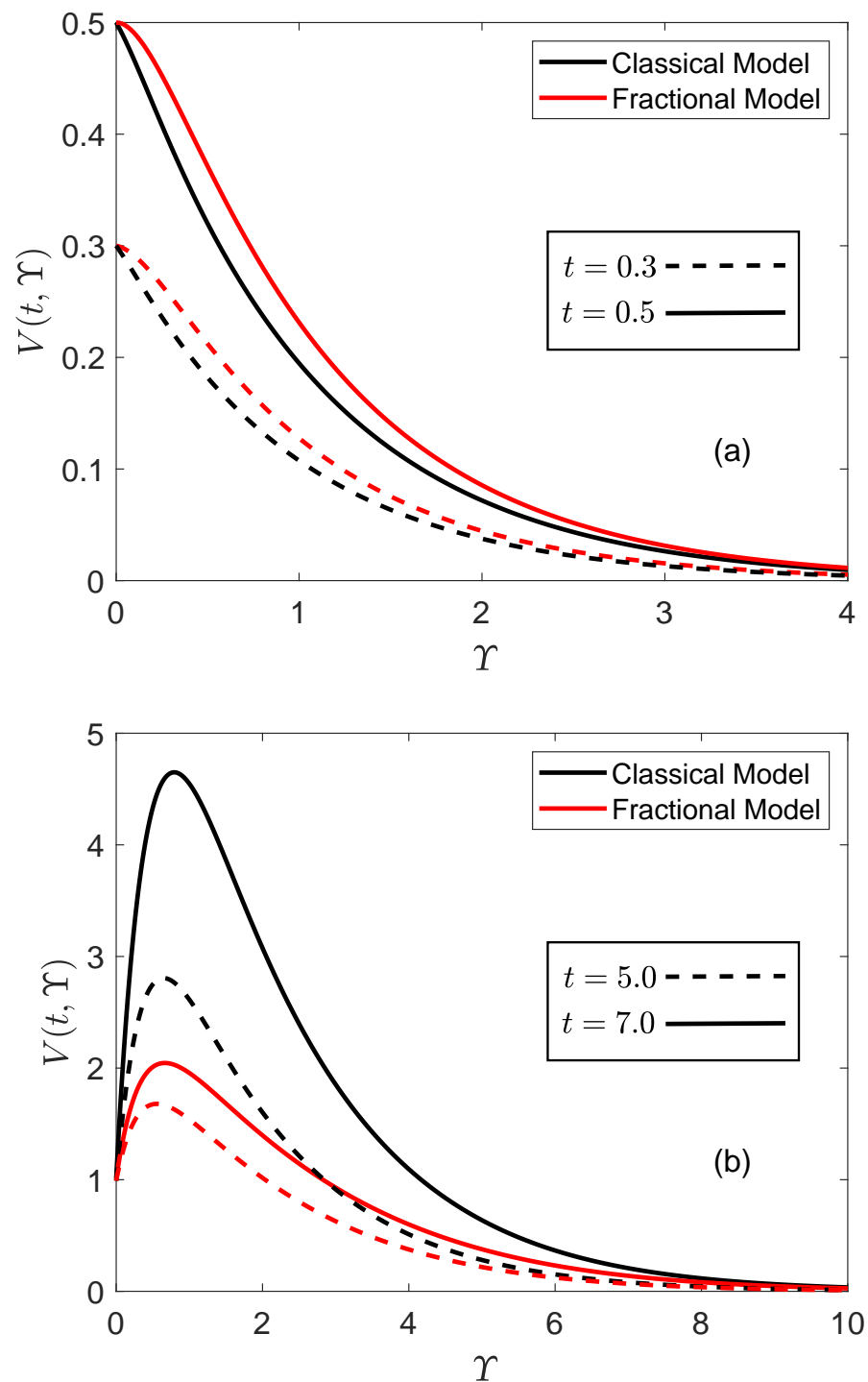
Figure 15. (**a**) Flow profile corresponding to fractional and classical cases for smaller time inputs. (**b**) Flow profile corresponding to fractional and classical cases for larger time inputs.

The results of simulations for the Nusselt number (*Nu*) are enclosed in Table 4 to anticipate the improvement and growth percentage in the heat-transporting tendency of vacuum pump oil in correspondence to an increased proportion (φ) of alloy particles. The respective table describes that a slight enhancement in the loading range of particles eventuates significant amelioration in the thermal efficiency of the presented nanofluid. For the maximum loading range of alloy particles ($\varphi = 0.04$), the considered nanofluid performs 44.53% better than regular vacuum pump oil. This advancement in heat transfer

performance is quite substantial and justifies the usefulness of the considered nanofluid for impetuous cooling of conduits and expeditious disposal of redundant heat. Hence, highly sensitive thermal processes can be effectively managed by using nanofluids. Table 5 contains computational estimations of Nu to examine the participation of the shape factor in the betterment of the thermal impacts of the considered nanofluid. The highest and lowest Nu values are observed for blade- ($Nu = 2.1480$) and brick- ($Nu = 1.7700$) shaped alloy particles, respectively. While anticipating the improvement of thermal behavior with respect to percentage, it is discerned that alloy nanoparticles of brick-like shapes escalate the heat transportation rate of vacuum pump oil up to 19.10%. However, this escalation is 44.53%, 29.97%, and 25.56% for blade-, platelet-, and cylinder-shaped nanoparticles, respectively. These striking disparities in augmentation percentage subject to shape differences enlighten the significance of taking shape factors into account for practical applications. These outcomes also highlight that one of the major factors to strengthen the inadequate thermal attributes of carrier fluids is the shape of the distributed nano-sized particles. These results imply that leaving out the shape component in theoretical investigations reduces the usefulness of the provided findings for practical circumstances.

Table 4. Investigation of Nu and augmentation percentage for variation of φ.

φ	ψ	η	Ω	Nu	% Augmentation
0.00	0.2	0.5	0.9	1.4862	-
0.005	0.2	0.5	0.9	1.5622	5.11
0.01	0.2	0.5	0.9	1.6400	10.35
0.015	0.2	0.5	0.9	1.7197	15.71
0.020	0.2	0.5	0.9	1.8013	21.20
0.025	0.2	0.5	0.9	1.8849	26.83
0.03	0.2	0.5	0.9	1.9705	32.59
0.035	0.2	0.5	0.9	2.0582	38.49
0.040	0.2	0.5	0.9	2.1480	44.53

Table 5. Investigation of Nu for multiple shapes of nanoparticles.

φ	Nu			
	Cylinder	Brick	Blade	Platelet
0.010	1.5762	1.5538	1.6400	1.5912
0.015	1.6224	1.5884	1.7197	1.6452
0.020	1.6695	1.6236	1.8013	1.7003
0.025	1.7174	1.6593	1.8849	1.7564
0.030	1.7662	1.6956	1.9705	1.8137
0.035	1.8159	1.7325	2.0582	1.8721
0.040	1.8665	1.7700	2.1480	1.9317

The enhancement and diminution of Nu and C_f in response to the modification of parameters ψ, η, and Ω are discussed with the support of Tables 6 and 7. To thoroughly investigate the behavior of Nu and C_f, these tables are developed for $t = 0.5$ and $t = 7.0$. For proliferating variation of ψ and η, Table 6 divulges that Nu illustrates opposite behavior for greater and lower time inputs. For the former situation, the value of Nu declines, whereas for the latter situation, an increment in Nu is noted. Contrary to that, Nu follows

a uniform pattern for Ω. For both $t = 0.5$ and $t = 7.0$, the magnitude of Nu reduces in response to rising inputs of Ω. The variation in shear stress is analyzed by communicating the outcomes for numerical simulations of C_f via Table 7. The mathematical settings for this analysis are exactly the same as those mentioned for Table 6. It is evaluated that parameters ψ, η, and Ω control the shear stress in identical manners as they control the Nusselt number. For $t = 0.5$, the magnitude of C_f rises due to the alteration of ψ and η, and a reverse pattern is identified for a greater time value. However, a decline in the value of C_f takes place when Ω increases. The results in Tables 6 and 7 give prominence to the fact that the fractional system formulated in the presented work provides more effective control over the behavior of boundary layers in comparison to that of a classical system. Moreover, accurate accordance between experimental reports and theoretic results produced through such fractional systems can be established by appropriately altering the fractional parameters. The respective tables also describe that shear stress is strengthened and heat transfer occurs at an expeditious rate corresponding to time advancement. Engineers are concerned that high shear stress causes a plethora of difficulties with regard to the practical utilization of fluids during industrial processes, such as the fact that it demands significantly boosted pumping power. So, one of the important targets is minimizing shear stress by dint of practical and efficacious measures. For the current analysis, C_f appears to have a lower magnitude for the under-observation nanofluid than it does for pure vacuum pump oil. While taking the drawbacks of dominant shear stress into consideration, this finding suggests that the presented nanofluid is a viable replacement for traditional fluids. Additionally, significantly greater outcomes of Nu in the case of the nanofluid as equated to that of regular vacuum pump oil describe that the thermal efficiency of working nanofluid is comparatively higher. The aforementioned claim receives further endorsement from this comparative analysis.

Table 6. Investigation of Nu for various values of ψ, η, and Ω.

ψ	η	Ω	Nu	
			$t = 0.5$	$t = 7.0$
0.1	0.8	0.9	1.7563	1.9221
0.4	-		1.7608	1.8793
0.7	-		1.7658	1.7861
0.9	-	-	1.7701	1.7550
0.2	0.1	-	1.6629	2.9781
-	0.4	-	1.7081	2.4028
-	0.7	-	1.7476	2.0089
-	0.9	-	1.7649	1.8243
-	0.8	0.1	1.7788	2.7058
-	-	0.4	1.7707	2.6537
-	-	0.7	1.7628	2.6040
-	-	0.9	1.7576	2.5722

Table 7. Investigation of C_f for various values of ψ, η, and Ω.

ψ	η	Ω	C_f	
			$t = 0.5$	$t = 7.0$
0.1	0.8	0.9	0.2863	3.2052
0.4	-		0.3211	2.8217
0.7	-		0.3568	2.2613
0.9	-	-	0.3782	1.7696
0.2	0.1	-	0.0955	9.7889
-	0.4	-	0.2026	8.0036
-	0.7	-	0.3593	4.0280
-	0.9	-	0.4143	2.3205
-	0.8	0.1	0.4425	3.6520
-	-	0.3	0.3867	3.4328
-	-	0.5	0.3325	3.2259
-	-	0.8	0.2973	3.0945

5. Conclusions

In this work, a combination of vacuum pump oil and aluminum alloy nanoparticles is investigated to anticipate the escalation in thermal efficiency of vacuum pump oil because of the effective thermo-physical attributes of alloy nanoparticles. The shape of nanoparticles is highly critical as far as the thermal performance of the resulting nanofluid is concerned; therefore, this analysis is conducted for platelet, brick, cylinder, and blade shapes of the considered nanoparticles. For the first time, this combination of host fluid and nanoparticles is examined with a boundary condition that contains the temperature function and its gradient. For the case of the flow phenomenon, free convection and the ramped velocity function jointly contribute to starting the process. Initially, the considered problem is described in terms of a partially coupled system that contains energy and velocity equations. Later, this system is transmuted to the fractional environment using a generalized Fourier law. To accomplish the generalization purpose, a Prabhakar fractional operator is put into action. The target of acquiring exact solutions is achieved by introducing mathematical relations for thermo-physical features and unit-independent quantities in the basic model and then executing the Laplace transform. These analytic solutions are employed for the preparation of graphs and tables to study various essential phenomena such as variations in boundary layers, heat transfer, and shear stress. Some vital findings of this investigation are highlighted as follows:

- Vacuum pump oil's thermal efficiency can be augmented by 44% when aluminum alloy nanoparticles are added to it.
- The viscosity of vacuum pump oil enhances due to material features and various shapes of suspended alloy nanoparticles. This increasing variation leads to raising the boiling point of the nanofluid, which strengthens its heat-transporting capacity, and the nanofluid indicates a higher thermal stability.
- The graph of the flow function declines, corresponding to the growing loading range of nanoparticles, whereas the temperature field exhibits a contrary behavior.
- The skin friction coefficient can be effectively controlled by means of the generalized model, which is helpful in limiting shear stress.
- The dispersion of blade-shaped nanoparticles induces the maximum boost in the heat-transporting performance of vacuum pump oil.
- A dual behavior of velocity and thermal fields is observed for shorter and longer time intervals subject to modification of fractional parameters.

- In contrast to a classical model, a better explanation of heat flux is provided by the generalized Fourier law due to the memory effect of the fractional model.
- The considered nanofluid is significantly better than ordinary vacuum pump oil in terms of heat transfer performance. Moreover, the skin friction coefficient is minimum for the former fluid.
- Thermal and flow fields show the highest graphs for the blade-like shape of nanoparticles. However, the brick and platelet shapes produce the lowest curves for thermal and flow fields, respectively.
- It is perceived that the coupled use of the ramped velocity function and a generalized model helps to control the flow efficaciously. Furthermore, the management of practical operations in terms of temperature adjustments can be performed in a better way.

6. Future Research Directions

- This work can be conducted for two- or three-dimensional unsteady problems.
- This model can be modified to investigate flow and heat transfer phenomena in more complex geometries such as cylinder, wedge, or disk.
- The presented fractional approach can be applied to other models to evaluate the performance of different hybrid nanofluids.

Author Contributions: Conceptualization, T.A. and A.; methodology, S.M., T.A. and A.; software, T.A. and M.Y.; validation, S.M., A. and M.Y.; formal analysis, S.M. and M.Y.; investigation, T.A. and A.; resources, S.M. and A.; data curation, T.A. and M.Y.; writing—original draft preparation, T.A. and A.; writing—review and editing, S.M., T.A., A. and M.Y.; visualization, S.M., T.A. and A.; supervision, T.A. and M.Y.; project administration, S.M. and M.Y.; funding acquisition, S.M., T.A. and M.Y. All authors have read and agreed to the published version of the manuscript.

Data Availability Statement: Not applicable.

Conflicts of Interest: The authors declare no conflict of interest.

Nomenclature

V^*	Nanofluid velocity	$\top$	Nanofluid temperature
V_0	Reference velocity	λ_0, λ_1	Jeffery parameters
t_0	Characteristic time	$\top_\infty$	Ambient temperature
$\widehat{\rho}$	Density	$\widehat{\mathcal{K}}$	Thermal conductivity
$\widehat{\beta}$	Thermal expansion coefficient	$\widehat{v}$	Kinematic viscosity
$\widehat{\mu}$	Dynamic viscosity	$\widehat{\mathcal{C}}_p$	Specific heat capacity
Y^*	Space coordinate	φ	Volume proportion of nanoparticles
t^*	Time	τ^*	Viscous drag
q^*	Thermal flux	h	Heat transfer coefficient
g	Gravitational acceleration	p	Laplace parameter
$\top$	Unit-free temperature	Nu	Nusselt number
Y	Unit-free space coordinate	C_f	Skin friction coefficient
η, Ω, ψ	Fractional parameters	V	Unit-free velocity
q	Unit-free thermal flux	t	Unit-free time

References

1. Serrano, E.; Rus, G.; Garcia-Martinez, J. Nanotechnology for sustainable energy. *Renew. Sustain. Energy Rev.* **2009**, *13*, 2373–2384.
2. Debele, T.A.; Yeh, C.F.; Su, W.P. Cancer immunotherapy and application of nanoparticles in cancers immunotherapy as the delivery of immunotherapeutic agents and as the immunomodulators. *Cancers* **2020**, *12*, 3773.
3. Choi, S.U.S.; Eastman, J.A. *Enhancing Thermal Conductivity of Fluids with Nanoparticles*; Technical report; Argonne National Lab. (ANL): Argonne, IL, USA, 1995.

4.   Wen, T.; Zhu, G.; Jiao, K.; Lu, L. Experimental study on the thermal and flow characteristics of ZnO/water nanofluid in mini-channels integrated with ga-optimized ANN prediction and CFD simulation. *Int. J. Heat Mass Trans.* **2021**, *178*, 121617.

5.   Rizwan, M.; Hassan, M.; Makinde, O.D.; Bhatti, M.M.; Marin, M. Rheological modeling of metallic oxide nanoparticles containing non-Newtonian nanofluids and potential investigation of heat and mass flow characteristics. *Nanomaterials* **2022**, *12*, 1237.

6.   Sarwar, L.; Hussain, A. Flow characteristics of Au-blood nanofluid in stenotic artery. *Int. Commun. Heat Mass Transf.* **2021**, *127*, 105486.

7.   Wang, Y.; Qi, C.; Ding, Z.; Tu, J.; Zhao, R. Numerical simulation of flow and heat transfer characteristics of nanofluids in built-in porous twisted tape tube. *Powder Technol.* **2021**, *392*, 570–586.

8.   Acharya, N.; Mabood, F.; Shahzad, S.A.; Badruddin, I.A. Hydrothermal variations of radiative nanofluid flow by the influence of nanoparticles diameter and nanolayer. *Int. Commun. Heat Mass Transf.* **2022**, *130*, 105781.

9.   Salahuddin, T.; Sakinder, S.; Alharbi, S.O.; Abdelmalek, Z. A brief comparative study of gamma alumina—Water and gamma alumina—EG nanofluids flow near a solid sphere. *Math. Comput. Simul.* **2021**, *181*, 487–500.

10.   Uddin, I.; Ullah, I.; Ali, R.; Khan, I.; Nisar, K.S. Numerical analysis of nonlinear mixed convective MHD chemically reacting flow of Prandtl–Eyring nanofluids in the presence of activation energy and Joule heating. *J. Therm. Anal. Calorim.* **2021**, *145*, 495–505.

11.   Hussain, A.; Hassan, A.; Arshad, M.; Rehman, A.; Matoog, R.T.; Abdeljawad, T. Numerical simulation and thermal enhancement of multi-based nanofluid over an embrittled cone. *Case Stud. Therm. Eng.* **2021**, *28*, 101614.

12.   Islam, T.; Yavuz, M.; Parveen, N.; Fayz-Al-Asad, M. Impact of Non-Uniform Periodic Magnetic Field on Unsteady Natural Convection Flow of Nanofluids in Square Enclosure. *Fractal Fract.* **2022**, *6*, 101.

13.   Tawade, J.V.; Guled, C.N.; Noeiaghdam, S.; Gamiz, U.F.; Govindan, V.; Balamuralitharan, S. Effects of thermophoresis and Brownian motion for thermal and chemically reacting Casson nanofluid flow over a linearly stretching sheet. *Results Eng.* **2022**, *15*, 100448.

14.   Tamilzharasan, B.M.; Karthikeyan, S.; Kaabar, M.K.; Yavuz, M.; Özköse, F. Magneto mixed convection of Williamson nanofluid flow through a double stratified porous medium in attendance of activation energy. *Math. Comput. Appl.* **2022**, *27*, 46.

15.   Waqas, H.; Farooq, U.; Muhammad, T.; Manzoor, U. Importance of shape factor in Sisko nanofluid flow considering gold nanoparticles. *Alex. Eng. J.* **2022**, *61*, 3665–3672.

16.   Alqaed, S.; Mustafa, J.; Aybar, H.Ş.; Jamil, B.; Alharthi, M.A. Investigation of thermal entropy generation and nanofluid flow in a new heatsink with effect of nanoparticles shape. *Case Stud. Therm. Eng.* **2022**, *36*, 102198.

17.   Saranya, S.; Al-Mdallal, Q.M. Computational study on nanoparticle shape effects of Al_2O_3-silicon oil nanofluid flow over a radially stretching rotating disk. *Case Stud. Therm. Eng.* **2021**, *25*, 100943.

18.   Ellahi, R.; Hassan, M.; Zeeshan, A.; Khan, A.A. The shape effects of nanoparticles suspended in HFE-7100 over wedge with entropy generation and mixed convection. *Appl. Nanosci.* **2016**, *6*, 641–651.

19.   Saqib, M.; Khan, I.; Shafie, S.; Mohamad, A.Q. Shape effect on MHD flow of time fractional Ferro-Brinkman type nanofluid with ramped heating. *Sci. Rep.* **2021**, *11*, 3725.

20.   Zahmatkesh, I.; Sheremet, M.; Yang, L.; Heris, S.Z.; Sharifpur, M.; Meyer, J.P.; Ghalambaz, M.; Wongwises, S.; Jing, D.; Mahian, O. Effect of nanoparticle shape on the performance of thermal systems utilizing nanofluids: A critical review. *J. Mol. Liq.* **2021**, *321*, 114430.

21.   Berrehal, H.; Sowmya, G.; Makinde, O.D. Shape effect of nanoparticles on MHD nanofluid flow over a stretching sheet in the presence of heat source/sink with entropy generation. *Int. J. Numer. Methods Heat Fluid Flow* **2021**, *32*, 1643–1663.

22.   Anwar, T.; Kumam, P.; Shah, Z.; Sitthithakerngkiet, K. Significance of shape factor in heat transfer performance of molybdenum-disulfide nanofluid in multiple flow situations; A comparative fractional study. *Molecules* **2021**, *26*, 3711.

23.   Hussain, M.; Farooq, U.; Sheremet, M. Nonsimilar convective thermal transport analysis of EMHD stagnation Casson nanofluid flow subjected to particle shape factor and thermal radiations. *Int. Commun. Heat Mass Transf.* **2022**, *137*, 106230.

24.   Jiang, Y.; Wang, X.; Mahmoud, M.Z.; Elkotb, M.A.; Baloo, L.; Li, Z.; Heidarshenas, B. A study of nanoparticle shape in water/alumina/boehmite nanofluid flow in the thermal management of a lithium-ion battery under the presence of phase-change materials. *J. Power Sources* **2022**, *539*, 231522.

25.   Shi, Y.; Abidi, A.; Khetib, Y.; Zhang, L.; Sharifpur, M.; Cheraghian, G. The computational study of nanoparticles shape effects on thermal behavior of H_2O-Fe nanofluid: A molecular dynamics approach. *J. Mol. Liq.* **2022**, *346*, 117093.

26.   Podlubny, I. *Fractional Differential Equations: An Introduction to Fractional Derivatives, Fractional Differential Equations, to Methods of their Solution and Some of Their Applications*; Elsevier: Amsterdam, The Netherlands, 1998.

27.   Caputo, M.; Fabrizio, M. A new definition of fractional derivative without singular kernel. *Progr. Fract. Differ. Appl.* **2015**, *1*, 73–85.

28.   Atangana, A.; Baleanu, D. New fractional derivatives with nonlocal and non-singular kernel: Theory and application to heat transfer model. *Therm. Sci.* **2016**, *4*, 763–769.

29.   Garra, R.; Garrappa, R. The Prabhakar or three parameter Mittag–Leffler function: Theory and application. *Commun. Nonlinear Sci. Numer. Simul.* **2018**, *56*, 314–329.

30.   Danane, J.; Hammouch, Z.; Allali, K.; Rashid, S.; Singh, J. A fractional-order model of coronavirus disease 2019 (COVID-19) with governmental action and individual reaction. *Math. Methods Appl. Sci.* **2021**, 1–14. https://doi.org/10.1002/mma.7759

31.   Akgül, E.K.; Akgül, A.; Yavuz, M. New illustrative applications of integral transforms to financial models with different fractional derivatives. *Chaos Solitons Fractals* **2021**, *146*, 110877.

32. Siddique, I.; Tlili, I.; Bukhari, S.M.; Mahsud, Y. Heat transfer analysis in convective flows of fractional second grade fluids with Caputo—Fabrizio and Atangana—Baleanu derivative subject to Newtonion heating. *Mech. Time-Depend. Mater.* **2021**, *25*, 291–311.

33. Chen, C.; Rehman, A.; Riaz, M.B.; Jarad, F.; Sun, X.E. Impact of Newtonian heating via Fourier and Fick's laws on thermal transport of Oldroyd-B fluid by using generalized Mittag-Leffler kernel. *Symmetry* **2022**, *14*, 766.

34. Raza, A.; Khan, U.; Zaib, A.; Mahmoud, E.E.; Weera, W.; Yahia, I.S.; Galal, A.M. Applications of Prabhakar-like fractional derivative for the solution of viscous type fluid with Newtonian heating effect. *Fractal Fract.* **2022**, *6*, 265.

35. Abro, K.A.; Abdon, A. A computational technique for thermal analysis in coaxial cylinder of one-dimensional flow of fractional Oldroyd-B nanofluid. *Int. J. Ambient Energy* **2021**, *43*, 5357–5365.

36. Lin, Y.; Rehman, S.; Akkurt, N.; Shedd, T.; Kamran, M.; Qureshi, M.I.; Botmart, T.; Alharbi, A.N.; Farooq, A.; Khan, I. Free convective trickling over a porous medium of fractional nanofluid with MHD and heat source/sink. *Sci. Rep.* **2022**, *12*, 20778.

37. Sene, N. Second-grade fluid with Newtonian heating under Caputo fractional derivative: Analytical investigations via Laplace transforms. *Math. Mod. Num. Simu. Appl.* **2022**, *2*, 13–25.

38. Kaleem, M.M.; Usman, M.; Asjad, M.I.; Eldin, S.M. Magnetic field, variable thermal conductivity, thermal radiation, and viscous dissipation effect on heat and momentum of fractional Oldroyd-B bio nano-fluid within a channel. *Fractal Fract.* **2022**, *6*, 712.

39. Rajagopal, K.R.; Ruzicka, M.; Srinivasa, A.R. On the Oberbeck–Boussinesq approximation. *Math. Models Methods Appl. Sci.* **1996**, *6*, 1157–1167.

40. Hamilton, R.L.; Crosser, O.K. Thermal conductivity of heterogeneous two-component systems. *Ind. Eng. Chem. Fundam.* **1962**, *1*, 187–191.

41. El-Kabeir, S.M.M.; El-Zahar, E.R.; Modather, M.; Gorla, R.S.R.; Rashad, A.M. Unsteady MHD slip flow of a ferrofluid over an impulsively stretched vertical surface. *AIP Adv.* **2019**, *9*, 045112.

42. Saqib, M.; Khan, I.; Shafie, S. Shape effect in magnetohydrodynamic free convection flow of sodium alginate-ferrimagnetic nanofluid. *J. Therm. Sci. Eng. Appl.* **2019**, *11*, 041019.

43. Giusti, A.; Colombaro, I. Prabhakar-like fractional viscoelasticity. *Commun. Nonlinear Sci. Numer. Simulat.* **2018**, *56*, 138–143.

44. Polito, F.; Tomovski, Z. Some properties of Prabhakar-type fractional calculus operators. *Fract. Diff. Calc.* **2016**, *6*, 73–94.

45. Alklaibi, A.M.; Sundar, L.S. Performance of Fe_3O_4—Vacuum pump oil nanofluid in tube with wire coil inserts. *J. Thermophys. Heat Transf.* **2021**, *35*, 494–501.

46. Makinde, O.D.; Mahanthesh, B.; Gireesha, B.J.; Shashikumar, N.S.; Monaledi, R.L.; Tshehla, M.S. MHD nanofluid flow past a rotating disk with thermal radiation in the presence of aluminum and titanium alloy nanoparticles. *Defect Diffus. Forum* **2018**, *384*, 69–79.